

# DETECTION OF AN INNER GASEOUS COMPONENT IN A HERBIG Be STAR ACCRETION DISK: NEAR- AND MID-INFRARED SPECTROINTERFEROMETRY AND RADIATIVE TRANSFER MODELING OF MWC 147<sup>1</sup>

STEFAN KRAUS, THOMAS PREIBISCH, AND KEIICHI OHNAKA

Max Planck Institut für Radioastronomie, Auf dem Hügel 69, 53121 Bonn, Germany; skraus@mpifb-bonn.mpg.de

Received 2007 April 11; accepted 2007 November 29

## ABSTRACT

We study the geometry and the physical conditions in the inner (AU-scale) circumstellar region around the young Herbig Be star MWC 147 using long-baseline spectrointerferometry in the near-infrared (NIR)  $K$ -band, VLT/AMBER observations, and PTI archive data, as well as the mid-infrared (MIR)  $N$ -band, VLT/MIDI observations. The emission from MWC 147 is clearly resolved and has a characteristic physical size of  $\sim 1.3$  and  $\sim 9$  AU at 2.2 and 11  $\mu\text{m}$ , respectively (Gaussian diameter). The MIR emission reveals asymmetry consistent with a disk structure seen under intermediate inclination. The spectrally dispersed AMBER and MIDI interferograms both show a strong increase in the characteristic size toward longer wavelengths, much steeper than predicted by analytic disk models assuming power-law radial temperature distributions. We model the interferometric data and the spectral energy distribution of MWC 147 with two-dimensional, frequency-dependent radiation transfer simulations. This analysis shows that models of spherical envelopes or passive irradiated Keplerian disks (with vertical or curved puffed-up inner rim) can easily fit the SED, but predict much lower visibilities than observed; the angular size predicted by such models is 2–4 times larger than the size derived from the interferometric data, so these models can clearly be ruled out. Models of a Keplerian disk with optically thick gas emission from an active gaseous disk (inside the dust sublimation zone), however, yield a good fit of the SED and simultaneously reproduce the absolute level and the spectral dependence of the NIR and MIR visibilities. We conclude that the NIR continuum emission from MWC 147 is dominated by accretion luminosity emerging from an optically thick inner gaseous disk, while the MIR emission also contains contributions from the outer, irradiated dust disk.

*Subject headings:* accretion, accretion disks — stars: formation — stars: individual (MWC 147) — stars: pre-main-sequence — techniques: interferometric

*Online material:* color figures

## 1. INTRODUCTION

The spatial structure of the circumstellar material around Herbig Ae/Be (HAeBe) stars, i.e., intermediate-mass, pre-main-sequence stars, is still a matter of debate. Until recently, the spatial scales of the inner circumstellar environment (a few AU, corresponding to  $\lesssim 0''.1$ ) were not accessible to optical and infrared imaging observations, and conclusions drawn on the spatial distribution of the circumstellar material were, in most cases, entirely based on the modeling of the spectral energy distribution (SED). However, fits to the observed SEDs are highly ambiguous, and very different models such as spherical envelopes (Miroshnichenko et al. 1997), geometrically thin disks (Hillenbrand et al. 1992), disks surrounded by a spherical envelope (Natta & Kruegel 1995; Natta et al. 2001; Miroshnichenko et al. 1999), flared outer disks, puffed-up inner disk rims (Dullemond et al. 2001), and disk plus inner halo models (Vinković et al. 2006) have been used to successfully fit the observed SEDs of HAeBes. It was also unclear how the accretion of circumstellar material onto the star affects the structure and emission of the inner circumstellar environment.

In the last couple of years, long-baseline interferometry in the near-infrared (NIR) and mid-infrared (MIR) spectral range provided, for the first time, direct spatial information on the *inner* circumstellar regions of young stars at scales of  $\lesssim 10$  mas (e.g.,

Malbet et al. 1998, 2007; Millan-Gabet et al. 1999, 2001; Akeson et al. 2000; Wilkin & Akeson 2003; Eisner et al. 2004; Leinert et al. 2004; Monnier et al. 2005). The interferometric data were usually interpreted by fitting simple analytic models for the brightness distribution to the measured visibilities. The characteristic sizes of the emitting regions derived in this way were found to be correlated to the stellar luminosity, consistent with the idea that the NIR continuum emission mainly traces hot dust close to the dust sublimation radius, i.e., where the grains are heated above their sublimation temperature ( $T_{\text{sub}} \sim 1500$  K) and destroyed by the (stellar) radiation field (Tuthill et al. 2002; Monnier & Millan-Gabet 2002). While the expected simple  $R_* \propto L_*^{1/2}$  scaling law between stellar luminosity  $L_*$  and NIR size  $R_*$  appears to hold throughout the low- to medium-luminosity part of the observed stellar sample, some very luminous early B-type stars exhibited considerably smaller NIR sizes than predicted by this relation (Monnier & Millan-Gabet 2002; Eisner et al. 2004; Monnier et al. 2005). Monnier & Millan-Gabet (2002) suggested that this might be due to the presence of an inner gaseous disk, which shields the dust disk from the strong stellar ultraviolet (UV) radiation. Since this shielding would be most efficient for hot stars, it would allow the inner rim of the dust disk around B-type stars to exist closer to the star. Several subsequent studies favor “classical” accretion disk models (Eisner et al. 2004; Monnier et al. 2005; Vinković & Jurkić 2007) or “two-ring” models (Eisner et al. 2007), in which the infrared emission contains contributions from the thermal emission of optically thick gas in the innermost disk regions.

Following initial attempts by Hinz et al. (2001), who used single-dish nulling interferometry to put upper limits of  $\lesssim 20$  AU on the

<sup>1</sup> Based on observations made with ESO telescopes at the La Silla Paranal Observatory under program IDs 074.C-0181, 076.C-0138, and 078.C-0129. In addition, this work is based in part on archival data obtained with the Spitzer Space Telescope, which is operated by the Jet Propulsion Laboratory, California Institute of Technology under a contract with NASA.

TABLE 1  
STELLAR PARAMETERS FOR MWC 147 FROM HERNÁNDEZ ET AL.  
2004 ASSUMING  $R_V = 3.1$

Parameter	Value
Spectral Type .....	B6
$T_{\text{eff}}$ .....	14,125 K
$L_*$ .....	$1550 L_{\odot}$
$M_*$ .....	$6.6 M_{\odot}$
Age $t$ .....	0.32 Myr
Distance $d$ .....	800 pc
$A_V$ .....	1.2 mag
$R_*$ .....	$6.63 R_{\odot}$

MIR size of some Herbig Ae stars, a large sample of HAeBes disks could be resolved with the VLTI/MIDI long-baseline interferometer at MIR wavelengths. In contrast to the NIR flux, which originates from hot dust in the innermost disk regions close to the dust sublimation radius, the MIR emission also traces cooler ( $\sim 200$ – $300$  K) dust further out in the disk. Leinert et al. (2004) determined characteristic dimensions of the  $10 \mu\text{m}$  emitting regions for a sample of HAeBes, which ranged from 1 to 10 AU.

Due to the quite limited  $uv$ -plane coverage of most existing infrared interferometric data sets, most published studies were only able to derive estimates of characteristic sizes and, in some cases, to look for possible elongation of the emitting region, but could not investigate the geometry of individual sources in detail. A more comprehensive interferometric study of one Herbig Ae star, HR 5999, was recently performed by our group (Preibisch et al. 2006). Based on a set of 10 MIDI measurements at different projected baseline lengths and position angles (P.A.s), modeling with two-dimensional frequency-dependent radiation transfer simulations provided relatively detailed information on the disk size and inclination.

In this study, we combine, for the first time, NIR and MIR interferometric observations to constrain the spatial structure of the dust and gas environment around a Herbig Be star. Besides the wide spectral coverage (from  $\sim 2$  to  $13 \mu\text{m}$ ), our interferometric data is also dispersed into several spectral channels (resolution  $R = \lambda/\Delta\lambda \approx 30$ ), allowing us to measure the wavelength dependence of the visibility over the  $K$ - and  $N$  bands and within spectral features such as the silicate emission feature around  $10 \mu\text{m}$ . In combination with detailed two-dimensional radiative transfer modeling, this spectrophotometric data set provides unique information about the inner circumstellar structures of this star.

MWC 147 (alias HD 259431, BD +10 1172, HBC 529, V700 Mon) is a well-studied Herbig Be star in Monoceros. There is some uncertainty concerning the distance and the physical parameters of this star. From the analysis of the *Hipparcos* parallax data by van den Ancker et al. (1998) a lower limit on the distance of  $>130$  pc was derived, while a reanalysis suggested a distance of  $290_{-84}^{+200}$  pc (Bertout et al. 1999). This distance estimate, however, is in conflict with the apparent location of MWC 147 in the NGC 2247 dark cloud, which is a part of the cloud complex in the Monoceros OB1 association at a distance of  $\sim 800$ – $900$  pc (Oliver et al. 1996). We assume a distance of 800 pc for MWC 147 (consistent with most other recent studies) and use the main stellar parameters as listed in Table 1, which were taken from Hernández et al. (2004).

Numerous observational results strongly suggest the presence of a circumstellar disk around MWC 147. The object shows a strong infrared excess of about 6 mag at MIR wavelengths, clearly demonstrating the presence of circumstellar material.

Hillenbrand et al. (1992) fitted the SED of MWC 147 with a model assuming an accretion disk and estimated an accretion rate of  $\dot{M}_{\text{acc}} = 1.01 \times 10^{-5} M_{\odot} \text{ yr}^{-1}$ . MIR (10 and  $18 \mu\text{m}$ ) imaging observations revealed an elongated diffuse emission component around MWC 147 along P.A.  $\sim 50^\circ$ , extending out to  $\sim 6''$  and contributing  $\sim 34\%$  to the total flux (Polomski et al. 2002). Mannings (1994) determined the 1.1 mm flux of MWC 147 and estimated the mass in the circumstellar disk/envelope to be  $<0.09 M_{\odot}$ . The study of the far-UV spectrum of MWC 147 by Bouret et al. (2003) also suggested the presence of a flared circumstellar disk. Polomski et al. (2002) imaged MWC 147 in the MIR and concluded that the star is surrounded by a moderately flared disk and probably an extended envelope. Measurements by Jain et al. (1990) showed a significant amount of linear polarization ( $\sim 1\%$  along P.A.  $\sim 106^\circ$ ) but no wavelength dependence of the polarization. The high observed rotational velocity of  $v \sin i = 90 \text{ km s}^{-1}$  (Boehm & Catala 1995) suggests a high inclination of the rotation axis of MWC 147 with respect to the line of sight. This implies that the orientation of the circumstellar disk should be closer to edge-on than to face-on.

Recently, Brittain et al. (2007) presented a high-resolution NIR spectrum of MWC 147, showing a strong Br $\gamma$  emission line. Using an empirical relation between the Br $\gamma$  luminosity and the accretion rate (as derived from UV veiling; van den Ancker 2005), they derive a mass accretion rate of  $\dot{M}_{\text{acc}} = 4.1 \times 10^{-7} M_{\odot} \text{ yr}^{-1}$ . As discussed in their § 5.2, it is well possible that this method underestimates the true mass accretion rate. Adopting the stellar parameters used in our study (Table 1) will also result in a larger value for the derived accretion rate.

Evidence for a strong stellar wind from MWC 147 comes from the observed P Cygni profiles in several emission lines (Bouret et al. 2003). A quantitative modeling of FUSE spectra revealed multiple absorption components with different temperatures, consistent with a flared disk interpretation (Bouret et al. 2003). Based on the intensity ratio of infrared hydrogen lines, Nisini et al. (1995) estimated a mass loss rate of  $2.0 \pm 0.4 \times 10^{-7} M_{\odot} \text{ yr}^{-1}$ , which is slightly higher than the mass loss rates determined from radio observations ( $0.68 \times 10^{-7} M_{\odot} \text{ yr}^{-1}$ ; Skinner et al. 1993).

The star has a faint visual companion at a projected separation of  $3''.1$  ( $\sim 2500$  AU,  $\Delta R = 6.82$ ; Baines et al. 2006). While Vieira & Cunha (1994) classified MWC 147 as a spectroscopic binary with a period of about 1 yr, this claim could not be confirmed in more recent observations (Corporon & Lagrange 1999).

First interferometric measurements on MWC 147 were presented by Millan-Gabet et al. (2001), providing an upper limit on the  $H$ -band size. Akeson et al. (2000) observed MWC 147 with the Palomar Testbed Interferometer (PTI) and resolved its emission in the  $K$  band at baselines around 100 m. They derived a best-fit Gaussian FWHM diameter of 1.38 mas ( $=1.1$  AU) in the  $K$  band.

## 2. OBSERVATIONS AND DATA REDUCTION

Details of all interferometric observations of MWC 147 used in this paper are summarized in Table 2. All visibility measurements were corrected for atmospheric and instrumental effects using calibrator stars observed during the same night. The calibrator stars as well as their assumed angular diameters are listed in Table 3. Figure 1 shows the  $uv$ -plane coverage obtained with these observations.

### 2.1. VLTI/MIDI Observations

The MIDI interferometer (Przygodda et al. 2003; Leinert et al. 2004) at the ESO Very Large Telescope Interferometer (VLTI) records spectrally dispersed interferograms in the  $N$  band ( $8$ – $13 \mu\text{m}$ ).

TABLE 2  
OBSERVATION LOG FOR INTERFEROMETRIC OBSERVATIONS ON MWC 147

INSTRUMENT	DATE (UT)	HOUR ANGLE	BAND/SPECTRAL MODE	BASELINE	PROJECTED BASELINE		CALIBRATORS	REFERENCE
					Length (m)	P.A. (deg)		
Near-Infrared								
IOTA/FLOUR.....	1998		<i>H</i>	38 m	~22	~25	See reference	1
IOTA/FLOUR.....	1998		<i>K'</i>	38 m	~21	~15	See reference	1
PTI.....	1999, 2000, 2003	<0 ≥0	<i>K</i>	NS NS	105.1 98.9	29 17	HD 42807, HD 43042, HD 43587, HD 46709, HD 50692	2, 3
PTI.....	2004		<i>K</i>	NW	85.7	76	HD 43042, HD 46709 HD 50692	3
PTI.....	2003, 2004	<0 ≥0	<i>K</i>	SW SW	78.6 84.4	154 143	HD 42807, HD 46709 HD 50692	
VLTI/AMBER.....	2006 Feb 20	03:14	<i>K/LR</i>	UT1-UT3	101.0	40	HD 45415	
Mid-Infrared								
VLTI/MIDI.....	2004 Oct 30	08:49	<i>N/PRISM</i>	UT2-UT4	89.4	82	HD 31421, HD 49161	
VLTI/MIDI.....	2004 Nov 1	05:23	<i>N/PRISM</i>	UT2-UT4	55.9	90	HD 25604, HD 49161, HD 31421	
VLTI/MIDI.....	2004 Dec 29	06:42	<i>N/PRISM</i>	UT2-UT3	46.5	46	HD 49161	
VLTI/MIDI.....	2004 Dec 30	02:33	<i>N/PRISM</i>	UT3-UT4	59.6	114	HD 49161	
VLTI/MIDI.....	2004 Dec 31	04:26	<i>N/PRISM</i>	UT3-UT4	61.5	108	HD 49161	
VLTI/MIDI (rej.).....	2005 Jan 1	05:43	<i>N/PRISM</i>	UT3-UT4	54.7	106	HD 31421, HD 49161	
VLTI/MIDI (rej.).....	2005 Feb 28	00:04	<i>N/PRISM</i>	UT2-UT3	39.3	44	HD 49161	
VLTI/MIDI.....	2007 Feb 8	05:41	<i>N/PRISM</i>	UT1-UT3	102.0	37	HD 49161	
VLTI/MIDI.....	2007 Mar 10	03:12	<i>N/PRISM</i>	UT1-UT2	56.4	35	HD 49161	

NOTE.—For more detailed information about the calibrator stars, refer to Table 3.

REFERENCES.—(1) Millan-Gabet et al. 2001; (2) reprocessing of data presented in Akeson et al. 2000; (3) Wilkin & Akeson 2003.

The MIDI observations of MWC 147 were carried out for ESO open time (OT) programs 074.C-0181 and 078.C-0129 (PI Th. Preibisch), using the NaCl prism as dispersive element (providing a spectral resolution of  $R = 30$ ) and the HIGH-SENS instrument mode. In total, nine observations were carried out on five different baseline configurations, as listed in Table 2.

TABLE 3  
CALIBRATOR STAR INFORMATION FOR THE INTERFEROMETRIC  
OBSERVATIONS PRESENTED IN TABLE 2

Star	<i>K</i>	<i>N</i> (Jy)	Spectral Type	$d_{UD,K}$ (mas)	$d_{UD,N}$ (mas)
HD 42807.....	4.85	0.5	G2 V	$0.45 \pm 0.03^a$	...
HD 43042.....	4.13	1.0	F6 V	$0.59 \pm 0.10^b$	...
HD 43587.....	4.21	1.0	F9 V	$0.48 \pm 0.30^c$	...
HD 45415.....	3.02	3.3	G9 III	$1.06 \pm 0.02^d$	...
HD 46709.....	2.62	4.4	K5 III	$1.66 \pm 0.02^d$	...
HD 50692.....	4.29	0.8	G0 V	$0.56 \pm 0.10^b$	...
HD 25604.....	2.03	7.2	K0 III	...	$1.96 \pm 0.08^e$
HD 31421.....	1.41	13.6	K2 IIIb	...	$2.58 \pm 0.15^e$
HD 49161.....	1.58	7.2	K4 III	...	$2.88 \pm 0.17^e$

NOTE.—The *V*-band magnitudes were taken from SIMBAD, the *K*-band magnitudes from the 2MASS point source catalog, and the *N*-band (12  $\mu$ m) flux density from Helou & Walker (1988).

<sup>a</sup> UD diameter from Malbet et al. (1998).

<sup>b</sup> UD diameter from the CHARM catalog Richichi & Percheron (2002).

<sup>c</sup> UD diameter adopted from Pasinetti Fracassini et al. (2001) using the *Hipparcos* parallax of 51.76 mas measured for HD 43587.

<sup>d</sup> UD diameter from Mérand et al. (2005).

<sup>e</sup> UD diameter from the CHARM2 catalog (Richichi et al. 2005).

We used the data reduction software package MIA+EWS<sup>2</sup> (release 1.5.1) to extract visibilities from the MIDI data. This package contains two independent data reduction programs, based on a coherent (EWS; Jaffe 2004) and an incoherent approach (MIA; Leinert et al. 2004). The reduction results obtained with both algorithms agree very well (within 3% for the calibrated visibility) for all data sets; with exception of the data sets from 2005 January–February. Inspection of the acquisition image for these specific data sets revealed a poor beam overlap; thus, we rejected them from our further analysis. The inspection of the acquisition images for the other data sets showed that the visual companion at a separation of 3.1'' was not in the MIDI field of view (FOV) and, therefore, does not affect the measured visibilities. The wavelength-dependent calibrated visibilities of the remaining seven data sets are shown in Figure 2. For the minimum relative error on the calibrated visibilities, we assume a conservative value of 10% (see Leinert et al. 2004).

## 2.2. VLTI/AMBER Observations

AMBER (Petrov et al. 2003, 2007), the NIR beam-combiner of the VLTI, can combine the light from up to three telescopes, providing not only the visibility amplitudes but also the closure phase relation. The observations of MWC 147 were conducted within OT program 076.C-0138 (PI Th. Preibisch) using the 8.2 m unit telescopes UT1-UT3-UT4. Spectrally dispersed interferograms were obtained in the low-resolution (LR) mode ( $R = 35$ ), which resolves the *K* band into 11 spectral channels. Due to problems with the fiber injection during that night, the flux reaching

<sup>2</sup> The MIA+EWS software package is available from <http://www.mpia-hd.mpg.de/MIDISOFT/>.

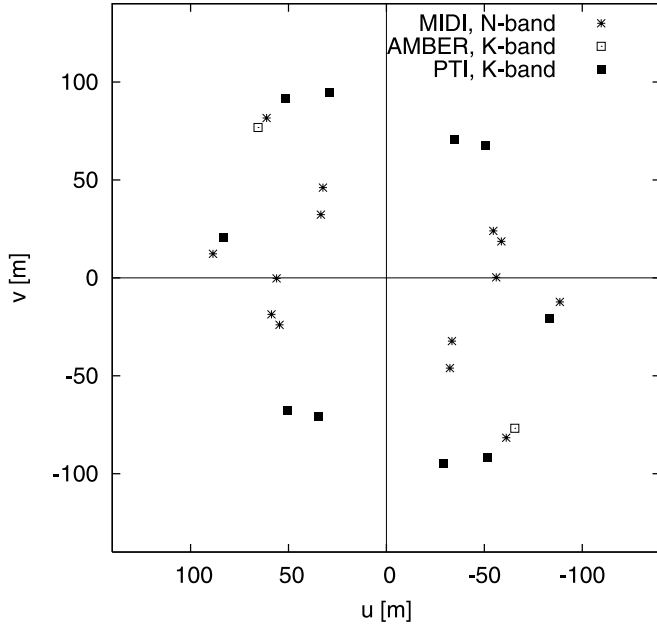


FIG. 1.— Plots of  $uv$ -plane coverage of the VLTI/MIDI, VLTI/AMBER, and archival PTI data. [See the electronic edition of the Journal for a color version of this figure.]

the AMBER beam combiner from UT4 was about a factor of 3 lower than from the other telescopes. Therefore, clear fringes were detectable on only one of the three baselines (UT1–UT3), and no closure phase signal could be measured. Following the ESO service mode observation procedure, one data set of 5000 interferograms was recorded both on a calibrator star (HD 45415) and on MWC 147. The length and orientation of the projected baseline for this AMBER measurement (101 m, P.A. =  $40^\circ$ ) is similar to the measurement at the PTI-NS baseline, but adds information about the spectral dependence of the visibility within the  $K$  band.

The AMBER data were reduced with version 2.4 of the `amdlib`<sup>3</sup> software employing the P2VM algorithm (Tatulli et al. 2007). Due to the absence of a fringe tracker, a large fraction of the interferograms is of rather low contrast (see discussion in Petrov et al. 2007). Therefore, we removed those frames from our data set for which (1) the light injection from the contributing telescopes was unsatisfying; i.e., the intensity ratio between

<sup>3</sup> The `amdlib` software package is available from <http://amber.obs.ujf-grenoble.fr>.

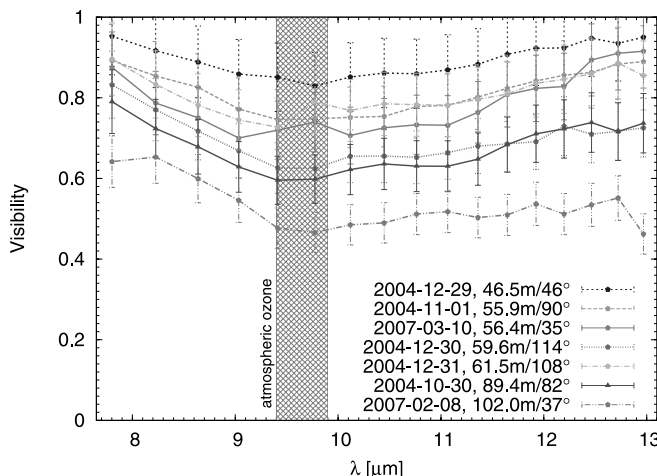


FIG. 2.— Visibilities measured with MIDI as a function of wavelength. [See the electronic edition of the Journal for a color version of this figure.]

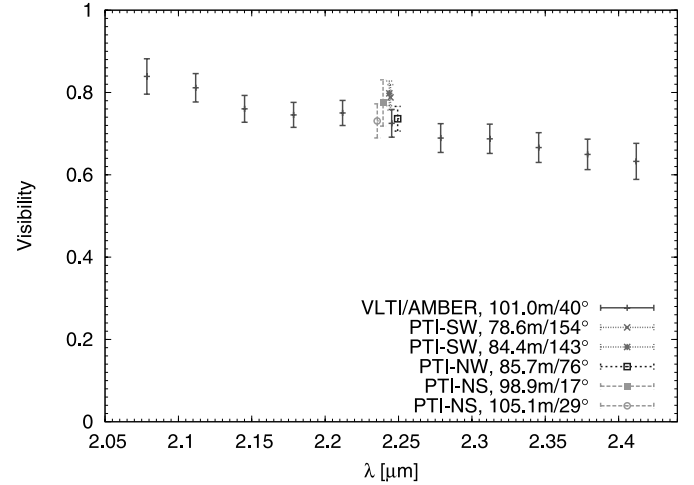


FIG. 3.— Wavelength dependence of the visibility measured with VLTI/AMBER and the visibilities measured with PTI using broadband filters. [See the electronic edition of the Journal for a color version of this figure.]

the photometric channels was larger than 4, (2) the atmospheric piston was larger than  $\frac{1}{4}$  of the coherence length  $\lambda \times R$ , or (3) the fringe contrast was decreased due to instrumental jitter (the 20% best interferograms were selected based on the Fringe SNR criteria, as defined in Tatulli et al. 2007). In Figure 3 the calibrated  $K$ -band visibilities derived from the AMBER and PTI measurements are shown as a function of wavelength. As mentioned in Petrov et al. (2007), the accuracy of the absolute calibration of the visibilities measured with VLTI/AMBER is currently limited by vibrations induced by the UTs, which lead us to assume a minimum relative error of 3% for the calibrated visibilities. In contrast to the absolute calibration, the wavelength-differential dependence of the visibility is insensitive to this effect (Petrov et al. 2007).

### 2.3. PTI Archive Data

MWC 147 was observed with the Palomar Testbed Interferometer (PTI; Colavita et al. 1999) on the NS (Akeson et al. 2000) and NS and NW baselines (Wilkin & Akeson 2003). Yet unpublished data for the SW baseline was retrieved from the PTI archive. To obtain a uniformly calibrated data set, we processed the new data set together with the previously published data using the V2Calib V1.4 software.<sup>4</sup> In the course of the calibration procedure, we applied to the raw visibilities (which were estimated from the spatially filtered PTI spectrometer output) the standard correction for coherence loss using the measured phase jitter (see Colavita et al. 1999). The individual PTI measurements were binned so that each bin contains data sets covering less than  $15^\circ$  variation along the P.A.. Since the measurements on the PTI-NS baseline also cover a relatively wide range of P.A.s ( $\sim 23^\circ$ ), we divided those measurements into two halves (depending on the P.A.) before averaging. As for the AMBER data, we assume 3% minimum relative error on the calibrated visibilities.

### 2.4. Spitzer-IRS Archive Data

In order to constrain the SED for our radiative transfer modeling as tightly as possible, we obtained MIR spectra from the *Spitzer Space Telescope* Archive. These spectra were recorded on 2004 October 26 within GTO program ID 3470 (PI: J. Bouwman) using the Infrared Spectrograph (IRS; Houck et al. 2004). The

<sup>4</sup> The V2Calib software is available from <http://msc.caltech.edu/software/V2calib/>.

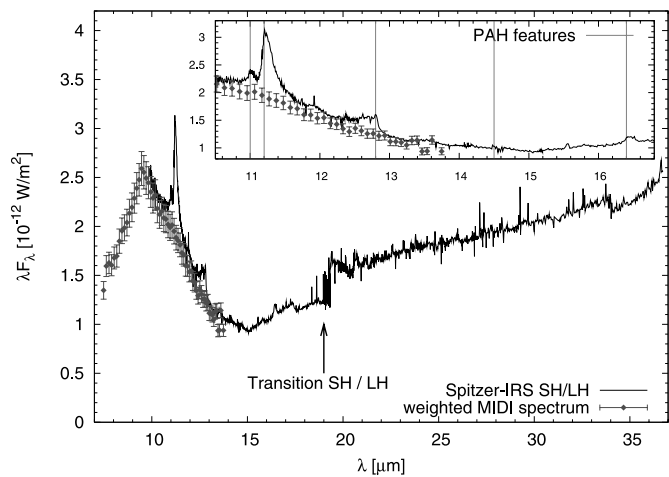


FIG. 4.— Comparison of the measured MIDI spectrum and the spectrum extracted from archival *Spitzer* IRS data. [See the electronic edition of the *Journal* for a color version of this figure.]

data set consists of four exposures; two taken in the Short-High mode (SH, wavelength range from 9.9 to 19.6  $\mu\text{m}$ ) and two in the Long-High mode (LH, 18.7 to 37.2  $\mu\text{m}$ ). Both modes provide a spectral resolution of  $R \sim 600$ . With slit sizes of  $4.7'' \times 11.3''$  (SH mode) and  $11.1'' \times 22.3''$  (LH mode), IRS integrates flux from areas much larger than those collected in the spatially filtered MIDI spectrum. The spectra were preprocessed by the S13.2.0 pipeline version at the *Spitzer* Science Center (SSC) and then extracted with the SMART software, version 5.5.7 (Higdon et al. 2004).

### 3. RESULTS

#### 3.1. The MIR Spectrum

In the overlapping wavelength regime between 10 and 13  $\mu\text{m}$ , the MIDI and *Spitzer*-IRS spectra show good quantitative agreement, both in the absolute level of the continuum flux and in the spectral slope (see Fig. 4). However, the IRS spectrum exhibits some line features which do not appear in the MIDI spectrum.<sup>5</sup> As these emission lines are most pronounced at wavelengths of 11.0, 11.2, 12.8, 14.5, and 16.4  $\mu\text{m}$ , we attribute these features to the presence of polycyclic aromatic hydrocarbons (PAHs; Allamandola et al. 1985; van Dishoeck 2004), which were found toward a large variety of objects, including T-Tauri stars and HAeBe stars (Acke & van den Ancker 2004). For the strong and rather broad emission feature at 11.2  $\mu\text{m}$ , contributions from the 11.3  $\mu\text{m}$  crystalline silicate feature are also possible.

The prominence of the PAH lines in the *Spitzer* IRS spectra with their  $4.7'' \times 11.3''$  FOV and their absence in the MIDI spectrum with its much ( $\sim 17\times$ ) smaller FOV suggests that the PAH emission comes predominantly from the outermost circumstellar environment and/or the surrounding nebulosity of MWC 147, similar to what was found for other young stellar objects (e.g., van Boekel et al. 2004b; Rho et al. 2006) or the outer regions of HAeBe disks (Habart et al. 2004, 2006).

The comparison of the *Spitzer*-IRS spectrum with the fluxes measured by IRAS (Helou & Walker 1988) showed that the IRAS fluxes are systematically higher. This is likely related to the larger

<sup>5</sup> In order to validate that the nondetection of the strong emission line around 11.2  $\mu\text{m}$  in the MIDI spectrum is not only due to MIDI's lower spectral resolution, we convolved the *Spitzer*-IRS spectrum to the resolution of the MIDI PRISM. Since the line is still clearly visible in the convolved spectrum, we are confident that no significant line emission is present in the spatially filtered MIDI spectrum.

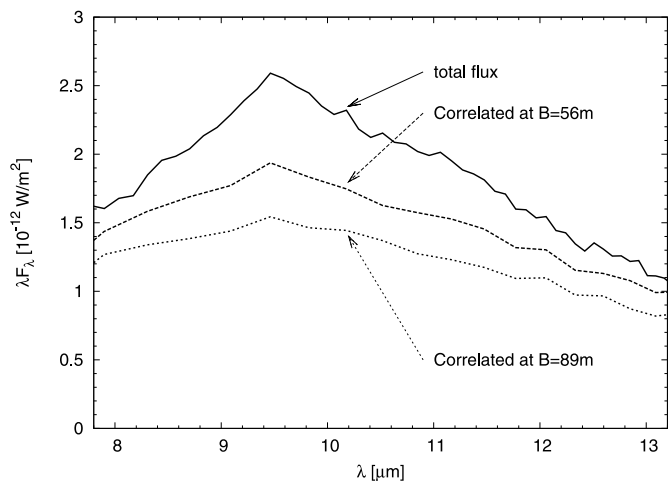


FIG. 5.— Total MIDI spectrum and the correlated flux at the 55.9 m (corresponding to a spatial scale of  $\lesssim 35$  AU) and 89.4 m ( $\lesssim 20$  AU) baselines. [See the electronic edition of the *Journal* for a color version of this figure.]

beam size of *IRAS*, which includes significant amounts of emission from the ambient NGC 2247 nebula. For our modeling in § 4, we will therefore treat the *IRAS* fluxes as upper limits only.

#### 3.2. The Correlated MIR Spectrum—Indications of Grain Growth

The visibilities measured with MIDI show significant variations along the recorded wavelength range. In particular, we detect a drop of visibility within the 10  $\mu\text{m}$  silicate feature. A similar behavior has already been observed for several HAeBe stars; e.g., in the samples of Leinert et al. (2004) and van Boekel et al. (2004a).

As the silicate emission feature is generally attributed to the presence of rather small silicate grains ( $r \lesssim 0.1 \mu\text{m}$ ; see, e.g., van Boekel et al. 2004a), it is possible to probe the radial dust mineralogy by comparing the correlated spectrum at various baseline lengths with the total spectrum  $F_{\text{tot}}$ . The correlated spectrum  $F_{\text{corr}}$  corresponds to the flux integrated over the spatial area unresolved by the interferometer for a particular baseline length  $B$ . Therefore, for each baseline length  $B$ , the correlated flux  $F_{\text{corr}}(B)$  can be computed by multiplying the total spectrum measured by MIDI in the photometry files with the visibility measured for a certain baseline. In order to probe the radial dependence of the dust mineralogy, measurements taken at similar P.A.s should be used in order to avoid contaminations by changes in the source geometry. We therefore choose the measurements from 2004 November 1 ( $B = 55.9$  m, P.A. =  $82^\circ$ ) and 2004 December 30 ( $B = 89.4$  m, P.A. =  $90^\circ$ ), as they have very similar P.A.s. The comparison of the correlated spectra for these baselines with the total spectrum (Fig. 5) shows that the 10  $\mu\text{m}$  silicate feature flattens out with increasing resolution. This change in the correlated spectrum might indicate spatial variations in the dust composition, with the more evolved dust grains (i.e., larger grains with a weaker silicate feature; Min et al. 2006) in the innermost disk regions.

#### 3.3. Geometric Model Fits

Since the imaging capabilities of the current generation of infrared interferometers are rather limited, the measured interferometric observables are often used to constrain the parameters of a model for the object morphology. In most studies presented until now, either purely geometric profiles (in particular uniform disk (UD) and Gaussian profiles) or physically motivated geometries such as ring profiles or analytic accretion disk models with a

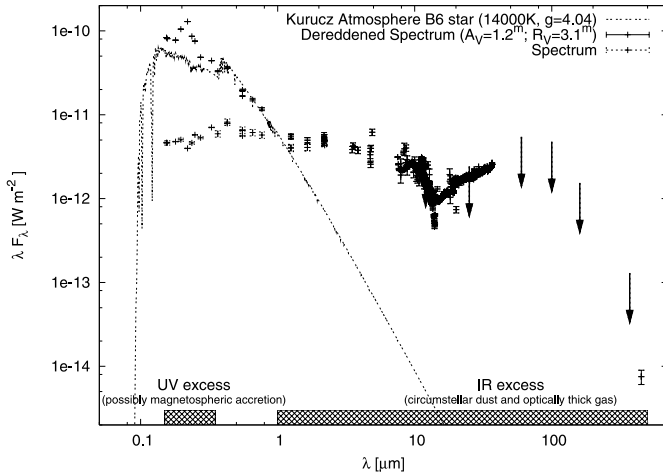


FIG. 6.— SED for MWC 147 containing the measured averaged, weighted MIDI spectrum, the archival *Spitzer* IRS spectrum and data from literature. Comparing the de-reddened SED with the Kurucz stellar atmosphere model for a B6 star reveals excess emission both in the UV and IR wavelength regime. The UV excess emission might originate in magnetospheric accretion (see the general models by Muzerolle et al. 2004), while the infrared excess likely indicates the presence of circumstellar dust and optically thick gas (see modeling in § 4). We included photometric data from Thompson et al. (1978; 156.5, 196.5, 236.5, and 274.0 nm), Wesseliuss et al. (1982; 150, 180, 220, 250, and 330 nm), Hillenbrand et al. (1992;  $U$ ,  $B$ ,  $V$ ,  $R_C$ ,  $I_C$ ,  $J$ ,  $H$ ,  $K$ ,  $L$ ,  $M$ ,  $N$ , and  $Q$  bands), Turon (1993;  $V$ -band), Egret et al. (1992;  $B$ -band), Høg et al. (2000;  $V_T$ ,  $B_T$ ,  $R_T$ , and  $I_T$  bands), Skrutskie et al. (2006; 2MASS;  $J$ ,  $H$ , and  $K_s$  bands), Cohen (1973; 2.2, 3.5, 3.65, 4.8, 4.9, 8.4, 8.6, 10.8, 11.0, 11.3, 12.8, and 18  $\mu\text{m}$ ), Polomski et al. (2002; 4.74, 7.91, 8.81, 10.27, 11.70, 12.49, 18.17  $\mu\text{m}$ , and  $N$ -band), Egan et al. (1999; MSX 2.6; 4.29, 8.28, 12.13, 14.65, and 21.34  $\mu\text{m}$ ), Berrilli et al. (1987; 2.2, 3.85, 8.65, 9.97, 10.99, and 11.55  $\mu\text{m}$ ), Helou & Walker (1988; 12, 25, 60, and 100  $\mu\text{m}$ ), Casey (1991; 160 and 370  $\mu\text{m}$ ), and Mannings (1994; 450  $\mu\text{m}$ ). [See the electronic edition of the *Journal for a color version of this figure.*]

power-law temperature distribution were employed. Ring models are justified by the theoretical expectation that most of the NIR emission originates from a rather small region around the dust sublimation radius (e.g., Millan-Gabet et al. 2001; Monnier & Millan-Gabet 2002).

A common problem in applying simple geometric models is that the observed emission does not originate exclusively from the circumstellar material: a certain fraction comes directly from the central star and contributes a spatially (nearly) unresolved component, and the existence of extended background emission, which is fully resolved, is also possible. For the model fits, one therefore has to specify which fraction of the total flux  $F_{\text{tot}}$  at any wavelength has to be attributed to the different spatial components. The stellar flux contribution  $f_{\text{star/tot}}(\lambda) = F_{\text{star}}/F_{\text{tot}}$  is often estimated from the SED, while the extended component  $f_{\text{ext/tot}}(\lambda) = F_{\text{ext}}/F_{\text{tot}}$  is usually assumed to be zero. These assumptions are, however, associated with a considerable uncertainty.

To allow comparison with earlier NIR interferometric studies on MWC 147, we keep the flux ratios from Millan-Gabet et al.

(2001), namely,  $f_{\text{star/tot}}(2.1 \mu\text{m}) = 0.16$ , and  $f_{\text{ext/tot}}(2.1 \mu\text{m}) = 0.0$  for the analytic fits. The same flux ratio was assumed by Wilkin & Akeson (2003), while Akeson et al. (2000) used  $f_{\text{star/tot}}(2.1 \mu\text{m}) = 0.10$ . At MIR wavelengths, the stellar contribution is likely to be negligible; i.e.,  $f_{\text{star/tot}}(10 \mu\text{m}) \approx 0$ . This can be concluded from the SED shown in Figure 6, where the infrared excess exceeds the stellar flux by a factor of  $\sim 280$  at 10  $\mu\text{m}$ .

### 3.3.1. Characteristic Source Size and Elongation

To obtain a first estimate of the object size, we fit the most common analytic profiles to our interferometric data: Gaussian, UD, and ring profiles. For mathematical descriptions of these profiles, we refer to Kraus et al. (2005; UD profile) and Millan-Gabet et al. (2001; Gaussian and ring profile). We assume uniform bright rings with an average diameter  $\Theta$  and a fixed width of 20% to be consistent with Monnier et al. (2005). As the apparent object size is expected to change with wavelength, we fitted these profiles to subsets of our data, covering wavelength ranges around 2.2, 8.6, 11.0, and 12.5  $\mu\text{m}$ . The visibilities measured in these subbands were fitted to the visibility profiles using a Levenberg-Marquardt least-square fitting algorithm, taking the chromatic change in resolution within the bandwidth into account.

The fits were performed for the case of circular symmetry (e.g., a disk seen face-on) and for elliptical structures (e.g., an inclined disk). The obtained diameters and goodness-of-fit values ( $\chi_r^2 = \sum [(V^2 - V_m^2)/\sigma_V]^2 / N_V$ , with  $V^2$  being the measured squared visibility,  $V_m^2$  the squared visibility computed from the model, and  $N_V$  the number of measurements) are given in Table 4 and 5. The  $\chi_r^2$  values already indicate that the elliptical geometries are a better representation of our data than the circular models. In order to illustrate this object elongation, we show the corresponding geometries in Figure 7. Since the detection of object elongation requires strict uniformity in the observational methodology, we did not include the single-baseline AMBER measurement because the mixture of broadband and spectrally dispersed interferometric observations might easily introduce artifacts.

While the elongation is only marginally evident in the PTI NIR measurements, it is more significant in the MIR data, although the limited P.A. coverage of the available MIDI data (covering  $\sim 80^\circ$  in P.A.) prevents us from measuring the precise axis ratio. The effect that the deviations from circular geometry seem to be stronger at MIR wavelengths might indicate that for the NIR model fits, the assumed stellar flux [ $f_{\text{star/tot}}(2.1 \mu\text{m}) = 0.16$ ] underestimates the real flux contributions from a spatially unresolved region (in agreement with our radiative transfer modeling results in § 4.4). For the MIR-interferometric data, it is interesting to note that the elongation found agrees well with the one seen in the 11.7/18.2  $\mu\text{m}$  color temperature map published by Polomski et al. (2002). Although these color temperature

TABLE 4  
MODEL FITS FOR CIRCULAR GEOMETRIES

GEOMETRY	K BAND		9 $\mu\text{m}$		11 $\mu\text{m}$		12.5 $\mu\text{m}$	
	Diameter (mas)	$\chi_r^2$	Diameter (mas)	$\chi_r^2$	Diameter (mas)	$\chi_r^2$	Diameter (mas)	$\chi_r^2$
Uniform disk (UD).....	2.6 $\pm$ 0.2	1.44	12.8 $\pm$ 2.0	1.38	17.3 $\pm$ 2.2	0.95	18.1 $\pm$ 2.2	0.89
Gaussian.....	1.6 $\pm$ 0.1	1.30	7.9 $\pm$ 1.4	1.19	10.8 $\pm$ 1.5	0.75	11.2 $\pm$ 1.5	0.90
Ring.....	1.8 $\pm$ 0.1	1.51	8.7 $\pm$ 1.4	1.49	11.8 $\pm$ 0.3	1.07	12.4 $\pm$ 1.3	0.90

NOTES.—For the  $K$ -band fits, we attribute 16% of the total flux to the unresolved stellar component. At a distance of 800 pc, 1 mas corresponds to 0.8 AU.

TABLE 5  
MODEL FITS FOR INCLINED GEOMETRIES

GEOMETRY	<i>K</i> BAND				9 $\mu\text{m}$				11 $\mu\text{m}$				12.5 $\mu\text{m}$			
	Diameter (mas)	<i>i</i> (deg)	P.A. (deg)	$\chi_r^2$	Diameter (mas)	<i>i</i> (deg)	P.A. (deg)	$\chi_r^2$	Diameter (mas)	<i>i</i> (deg)	P.A. (deg)	$\chi_r^2$	Diameter (mas)	<i>i</i> (deg)	P.A. (deg)	$\chi_r^2$
UD.....	3.0 $\times$ 2.4	39	12	0.33	20.1 $\times$ 10.8	58	58	1.04	20.8 $\times$ 15.3	43	53	0.59	23.5 $\times$ 15.7	48	70	0.58
Gaussian.....	1.8 $\times$ 1.4	39	11	0.30	18.5 $\times$ 6.5	69	66	0.89	23.3 $\times$ 8.9	68	65	0.31	23.5 $\times$ 9.0	68	74	0.49
Ring.....	2.1 $\times$ 1.6	41	12	0.34	14.0 $\times$ 7.5	58	60	1.06	20.2 $\times$ 10.1	60	66	0.48	16.3 $\times$ 10.9	48	64	0.59

NOTES.—The angle *i* denotes the inclination computed from the fitted axis ratio, assuming an underlying circular source structure. However, due to the unknown flux contribution from the unresolved central region (i.e., stellar flux, for which we assume  $f_{\text{star/tot}}(\text{NIR}) = 0.16$  and  $f_{\text{star/tot}}(\text{MIR}) = 0.0$ , and maybe additional accretion luminosity), and the incomplete P.A. coverage of the MIDI data set, we consider this value rather uncertain.

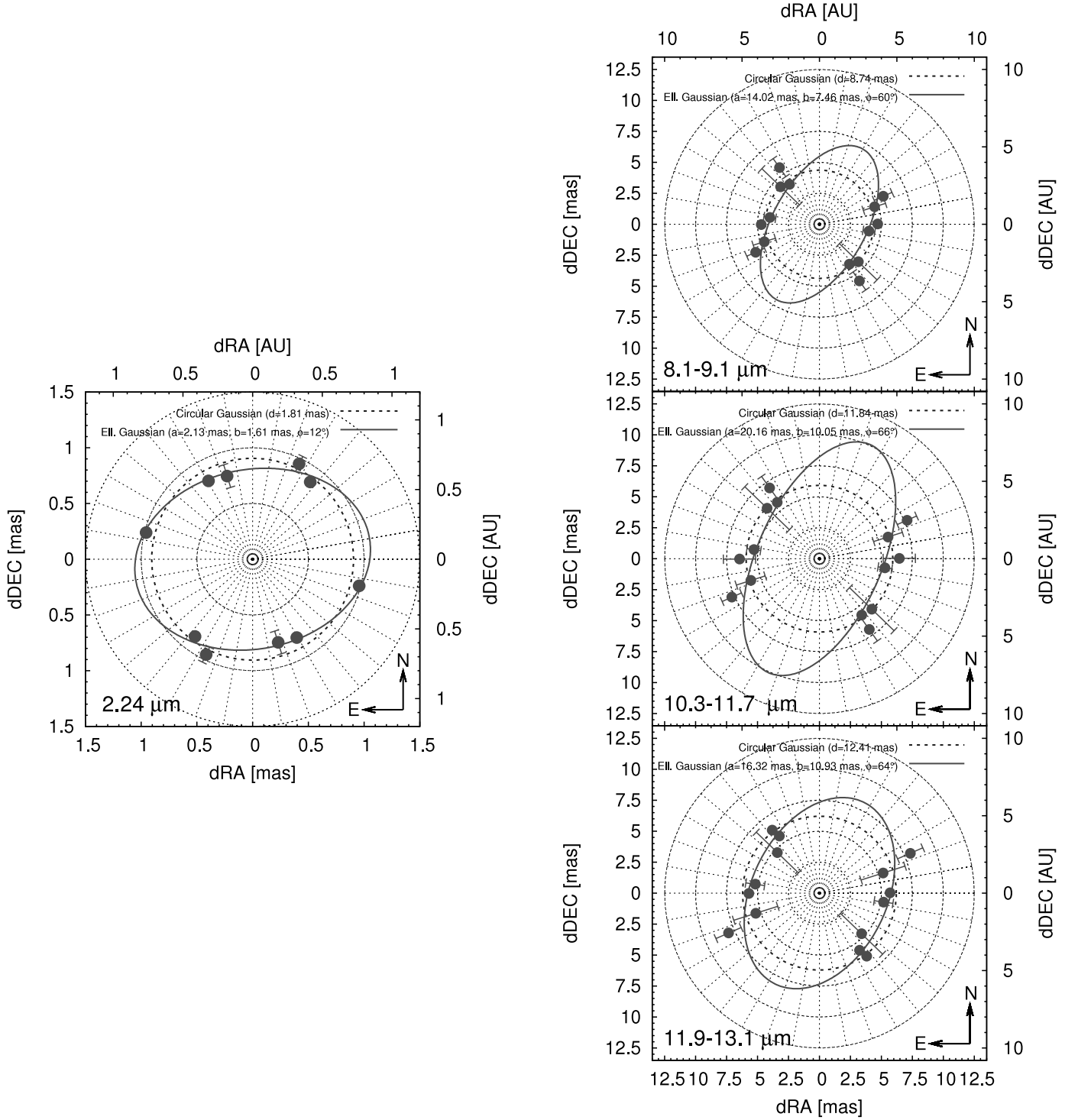


FIG. 7.— Polar diagram showing the best-fit circular and elliptical geometries. To derive the characteristic object size along different P.A.s (dots with error bars), we fitted ring profiles to the PTI  $K$ -band visibilities (left panel) and to MIDI visibilities (right panel) which were averaged over five spectral channels around the silicate feature (10.3–11.7  $\mu\text{m}$ ) and in the surrounding continuum ranges 8.1–9.1 and 11.9–13.1  $\mu\text{m}$ . [See the electronic edition of the Journal for a color version of this figure.]

maps show structures on scales of several arcseconds (e.g., on scales a hundred times larger than our interferometric data), their orientation ( $\sim 50^\circ$ ) and rough axis ratio are similar to those of the structure seen in our MIDI observations.

### 3.3.2. Wavelength-dependent Characteristic Size

Our combined MIDI/AMBER/PTI/IOTA data set also allows us to study the wavelength dependence of the apparent size. For this, we fitted the visibility measurement in each individual

spectral channel with the analytic formula for Gaussian intensity profiles (the result does not depend strongly on the assumed profile). The determined diameters are shown in Figure 8. The increase of the apparent size with wavelength is usually interpreted as a consequence of the radial temperature profile for the circumstellar material (i.e., material at larger distances from the star is cooler). However, as will be qualitatively discussed in § 3.4, the increase of the characteristic size with wavelength is much steeper than expected for single power-law temperature accretion disks

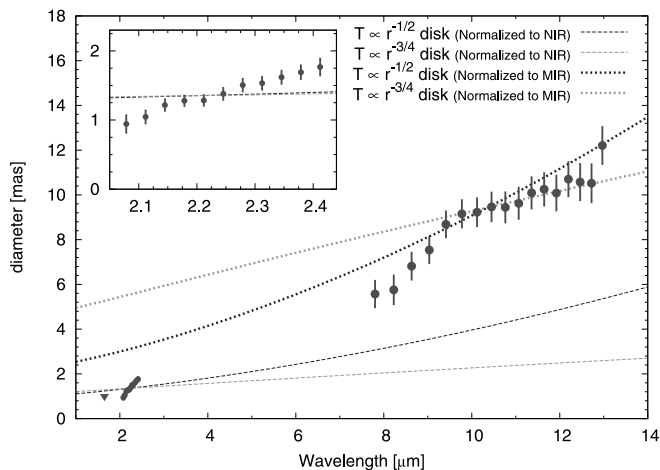


FIG. 8.— Wavelength dependence of the measured characteristic size over the  $H$ ,  $K$  and  $N$  bands, including IOTA, PTI, AMBER, and MIDI measurements. From our seven MIDI measurements, we choose the data set from 2007 February 8, since this measurement was taken at very similar baseline length and P.A. ( $102.0 \text{ m}/35^\circ$ ) as the AMBER data set ( $101.0 \text{ m}/40^\circ$ ), which makes these data sets particularly well suited to study the radial disk structure without contamination by the detailed source geometry. The IOTA  $H$ -band measurement provides only an upper size limit. To compute the characteristic size, Gaussian intensity profiles were assumed. For comparison, we show the wavelength-dependent size corresponding to the commonly applied analytic disk model from Hillenbrand et al. (1992). We scaled these disk models to match the measured NIR (*dashed curves*) or MIR size (*dotted curves*). In all cases, it is evident that these analytic models cannot describe the measured wavelength-dependent size well. [See the electronic edition of the *Journal* for a color version of this figure.]

with an inner hole, suggesting that these models cannot successfully explain the observed wavelength dependence of the emitting structure. In the context of our radiative transfer modeling in § 4, we will discuss that this discrepancy can be explained assuming the presence of an additional, more compact emitting region which dominates the emission at NIR wavelengths, but whose contribution becomes less important at MIR wavelengths.

Akeson et al. (2000) examined the possibility whether the measured visibilities could indicate the presence of a close companion. Since PTI observed MWC 147 several times over a period of  $\sim 4$  yr and found no significant variations on the NS baseline, we consider the binary scenario as very unlikely. For example, assuming, just for the sake of argument, a total system mass of  $7 M_\odot$  and a semimajor axis of 10 AU, this would give an orbital period of  $\sim 12$  yr and should result in significant visibility variations over the covered 4 yr.

### 3.4. Comparison with Analytic Disk Models

Analytical models, both of passive irradiating circumstellar disks (Friedjung 1985) as well as viscous, actively accreting disks (Lynden-Bell & Pringle 1974), predict that the radial temperature profile of YSO disks should follow a simple power-law  $T(r) \propto r^{-\alpha}$ . Most studies infer a power-law index of  $\alpha = 3/4$  (Millan-Gabet et al. 2001; Eisner et al. 2005) or  $1/2$  (e.g., Leinert et al. 2004). Using this radial temperature power law and the assumption that each disk annulus radiates as a blackbody, we can compute the wavelength dependence of the disk size corresponding to a certain analytic model. To model the wavelength dependence of the size of an accretion disk model with constant power law, we simulated disks with  $T(r) = r^{-\alpha}$ , where  $r$  is chosen to be in units of the disk inner radius with a temperature at the inner dust rim of  $T(1) \equiv 1500 \text{ K}$ . The outer disk radius is chosen so that the temperature drops well below 100 K. After computing the intensity profile, we determine the disk size  $a(\lambda)$  for these analytic disk models using the half-light radius definition by Leinert et al. (2004). Finally, we scale the half-light diameter to fit the NIR (or MIR) size measured on MWC 147 and show the resulting  $a(\lambda)$ -curves for the aforementioned representative values for  $\alpha$  (Fig. 8).

Hillenbrand et al. 1992 fitted the SEDs of HAeBe stars with analytic disk models that combined the temperature profile of the reprocessing and actively accreting disk component. This class of “classical” optically thick, geometrically thin accretion disk

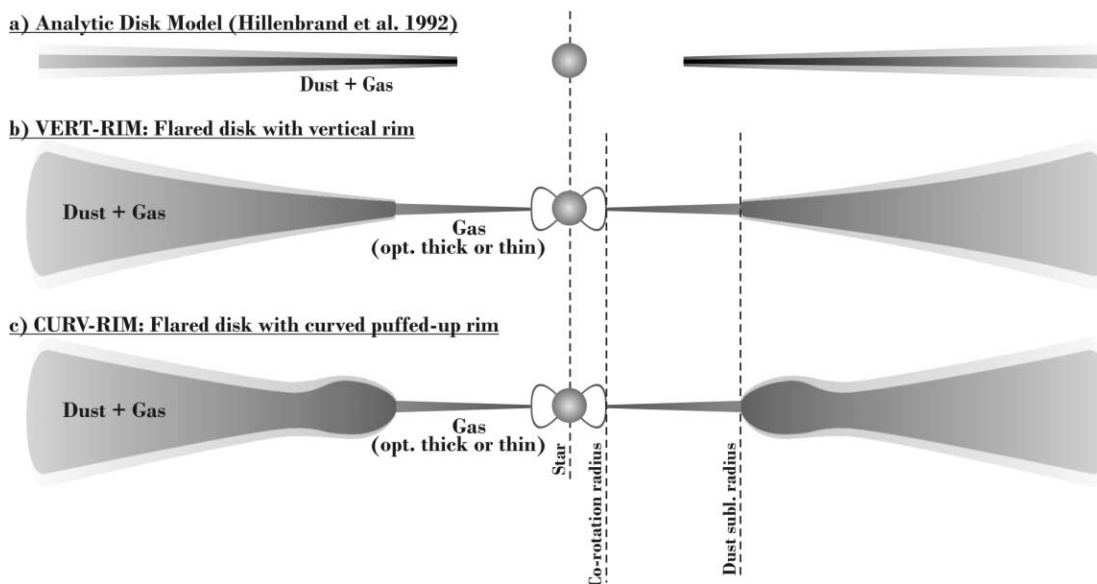


FIG. 9.— Illustration of the considered disk model geometries: (a) “Classical” accretion disk geometry as considered in the Hillenbrand et al. (1992) model (see § 3.4), incorporating an optically thick gas and dust disk. (b) In our models VERT-RIM and VERT-RIM-ACC, the dust component of the outer flared dust disk is truncated at the dust sublimation radius, while the gas located at smaller radii is either optically thin (model VERT-RIM, § 4.3) or optically thick (model VERT-RIM-ACC, § 4.4). (c) Due to direct stellar heating, the scale height at the inner dust rim might be increased, resulting in a puffed-up inner rim. Furthermore, various effects, such as a pressure-dependent dust evaporation temperature and dust segregation toward the disk midplane, will cause the rim to curve. We investigate the influence of such a curved rim shape in our models CURV-RIM (§ 4.3) and CURV-RIM-ACC (§ 4.4). [See the electronic edition of the *Journal* for a color version of this figure.]

models (Fig. 9a) was also favored by various authors to model the SED and NIR broadband visibilities of Herbig Be stars (Eisner et al. 2004; Monnier et al. 2005; Vinković & Jurkić 2007). Vinković & Jurkić (2007) modeled a large set of archival interferometric data and concluded that such classical accretion disk models are consistent with the observed visibilities of Herbig Be stars. Therefore, we examined whether such models can reproduce our combined NIR/MIR spectrophotometric data on MWC 147. In order to fit this analytic model with precisely the same procedure as for our radiative transfer modeling (§ 4.1.2), we computed the temperature profile using the equations given in Hillenbrand et al. (1992) and included the blackbody emission from an infinitely thin disk in our radiative transfer grid. Using the stellar parameters given in Table 1, we found that a disk model with the same parameters as derived by Hillenbrand et al. (1992) for this star (i.e., inner and outer disk radii of  $R_{\text{in}} = 12 R_{\star}$  and  $R_{\text{out}} = 62 \text{ AU}$ ) provides a good fit to the observed SED for an intermediate disk inclination angle ( $45^{\circ}$ , see § 3.3.1) and assuming a mass accretion rate of  $\dot{M}_{\text{acc}} \approx 4 \times 10^{-5} M_{\odot} \text{ yr}^{-1}$ . As shown in Figure 10, this model can also reproduce the absolute level of the NIR visibilities, but it fails to reproduce the spectral dependence of the VLTI/AMBER visibilities and also underestimates the MIR size, resulting in a rather high  $\chi_r^2$  of 5.56.

It is obvious that these analytic models cannot reproduce the measured NIR and MIR sizes simultaneously. To understand the strong increase in the apparent size with wavelength, contributions from the following effects might be of importance:

1. Analytic disk models generally do not include the effects of scattered light, which can provide significant heating of the outer parts of the disk and, thus, increase the apparent disk size at MIR wavelengths.
2. It has been suggested that the disks around YSOs may not be flat but flare with increasing radius. Such a flaring is expected from vertical hydrostatic equilibrium considerations (Kenyon & Hartmann 1987). As a result, the outer disk regions intercept more stellar flux, resulting in an increased luminosity and apparent size at MIR wavelengths.
3. The flux contribution from an extended cold envelope  $f_{\text{env/total}}(\lambda)$  might be nonnegligible in the MIR.
4. The NIR size might be underestimated, if the amount of NIR emission originating from close to the star is inadequately estimated [e.g., due to a biased  $f_{\text{star/disk}}(\lambda)$  or additional accretion luminosity].

This enumeration illustrates that the currently routinely applied analytic disk models contain several problematic points. A more physical and consistent approach requires detailed radiative transfer modeling. In the next section we present two-dimensional radiative transfer modeling for MWC 147.

## 4. TWO-DIMENSIONAL RADIATIVE TRANSFER SIMULATIONS

### 4.1. Modeling Procedure

#### 4.1.1. Monte Carlo Radiative Transfer Simulations

For a physical modeling of our interferometric data, we employ the radiative transfer code `mcsim_mpi` (author: K. Ohnaka), which solves the radiative transfer problem self-consistently using a Monte Carlo approach. This code is described in Ohnaka et al. (2006) and has been applied for the interpretation of interferometric data in Ohnaka et al. (2006) and Hönig et al. (2006). In short, the stellar flux is treated as a finite number of photon packets which are emitted in arbitrary directions. While

propagating through the cells of the simulation grid, the photon packet can be either scattered or absorbed. The probability of these events is given by the density and the optical properties of the dust in each particular cell. For scattering events, the propagation direction of the photon packet changes anisotropically, according to the Henyey-Greenstein function (this allows us to also properly treat scattering on large grains). For each absorption event, energy is deposited into the cell while the packet is isotropically reemitted immediately. The temperature of the cell is corrected using the scheme by Bjorkman & Wood (2001) resulting in a self-consistent determination of the dust temperature distribution. After tracing the propagation of a large number of photon packets through the simulation grid, the SED is computed by summing the flux from all packets. The code is parallelized using the LAM/MPI library, which allows the user to distribute the Monte Carlo computation on a large number of computers within a network. We extended the original `mcsim_mpi` code by adding an option to include the thermal emission from optically thick gas (see § 4.4).

As we require particularly high spatial resolution in the inner disk region to properly resolve the structure of the inner dust rim (at scales of a few AU) but also need to include structures with large radial extension (10,000 AU scale), we employed a spherical grid with logarithmic radial grid spacing. The number of radial cells was chosen to be 500, while the latitudinal grid resolution is  $1^{\circ}$ . We used  $5 \times 10^7$  photon packets per simulation, which ensures sufficient statistics for Monte Carlo radiative transfer.

As the input stellar spectrum, we use a Kurucz stellar atmosphere model (Kurucz 1970) for a B6-type star of solar metallicity ( $T_{\text{eff}} = 14,000 \text{ K}$ ,  $\log g = +4.04$ ). For the optical dust properties we use a mixture of warm silicate (Ossenkopf et al. 1992) and amorphous carbon (Hanner 1988) grains. The grain size distribution follows the dependence suggested by  $[n(a) \propto a^{-3.5}]$ , where  $a_{\text{min}} \leq a \leq a_{\text{max}}$  Mathis et al. 1977]. For the outer envelope, we use small grains ( $a_{\text{min}} = 0.005 \mu\text{m}$ ;  $a_{\text{max}} = 1.0 \mu\text{m}$ ), whereas for the inner disk region, we mix in larger dust grains ( $a_{\text{min}} = 1.0 \mu\text{m}$ ;  $a_{\text{max}} = 1000 \mu\text{m}$ ). The species of large and small grains are treated separately in the radiative transfer computations. A minimum dust density of  $10^{-25} \text{ g cm}^{-3}$  is assumed.

In order to avoid unrealistically sharp cutoffs at the outer edges of the considered density distributions, we used a Fermi-type function  $F(r_{\text{cutoff}})$  to obtain a smooth truncation of the density distribution around the radius  $r_{\text{cutoff}}$ :

$$F(r_{\text{cutoff}}) = \left[ 1 + \exp\left(\frac{r - r_{\text{cutoff}}}{\epsilon r_{\text{cutoff}}}\right) \right]^{-1}, \quad (1)$$

where  $\epsilon = 0.05$  defines the relative width of the transition region.

#### 4.1.2. Joint Fitting of the SED and Wavelength-dependent Visibilities

Once the radiative transfer computation is completed, a ray-trace program is used to compute the SED and synthetic images for any wavelength of interest. For this project, we compute synthetic images at three wavelengths in the  $H$  band, three wavelengths in the  $K$  band, and eight wavelengths in the  $N$  band. Finally, visibilities are computed from the simulated images for the points of the  $uv$ -plane covered by the data. In order to treat the visibility slope in the spectrophotometric observations properly, we compute the visibility for each spectral channel of the MIDI and AMBER observations separately, using the synthetic image computed for a wavelength as close as possible to the central wavelength of the spectral bin.

Besides the interferometric observables, we use the SED of MWC 147 (as shown in Fig. 6, including the *Spitzer*-IRS spectrum

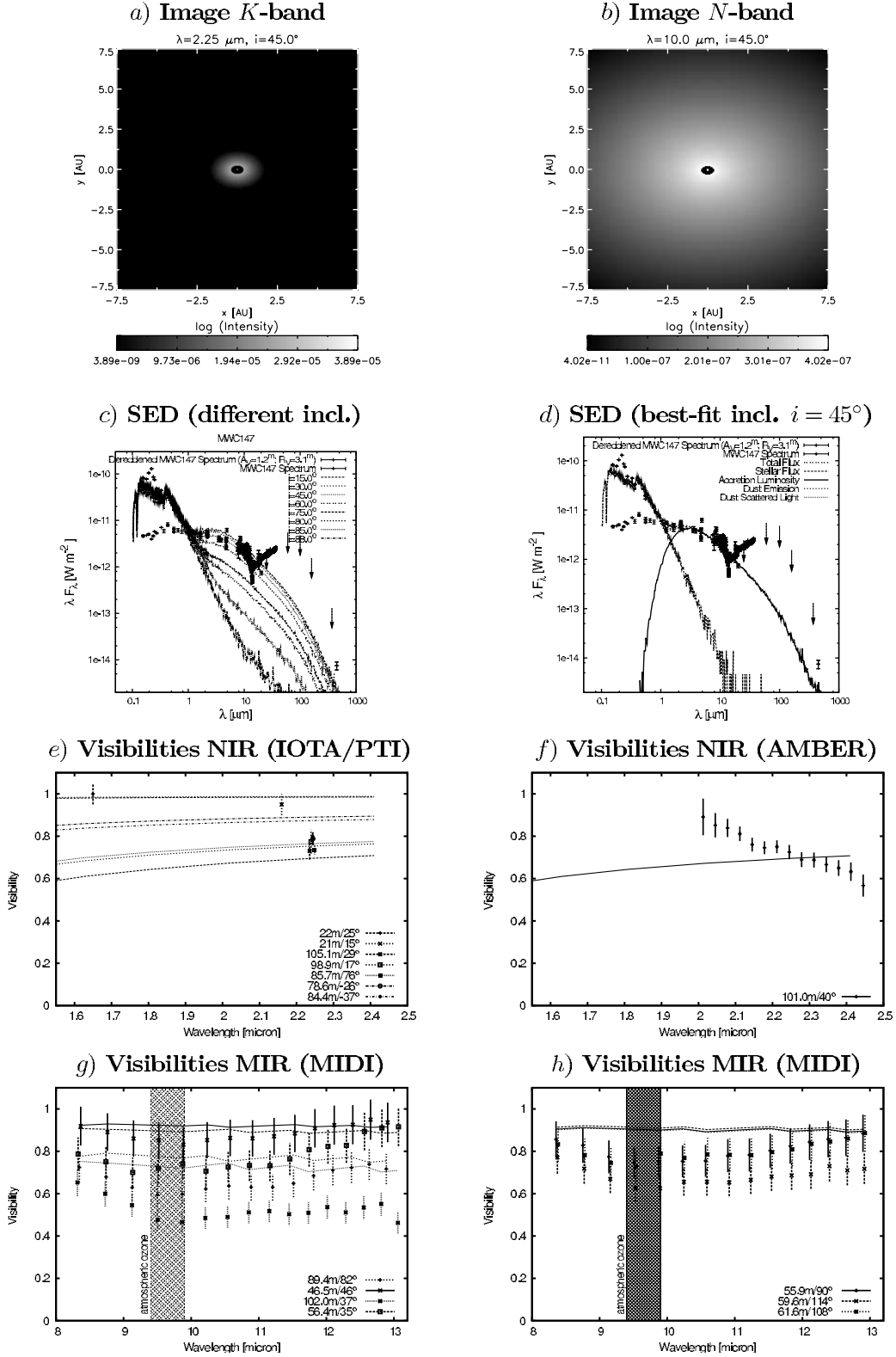
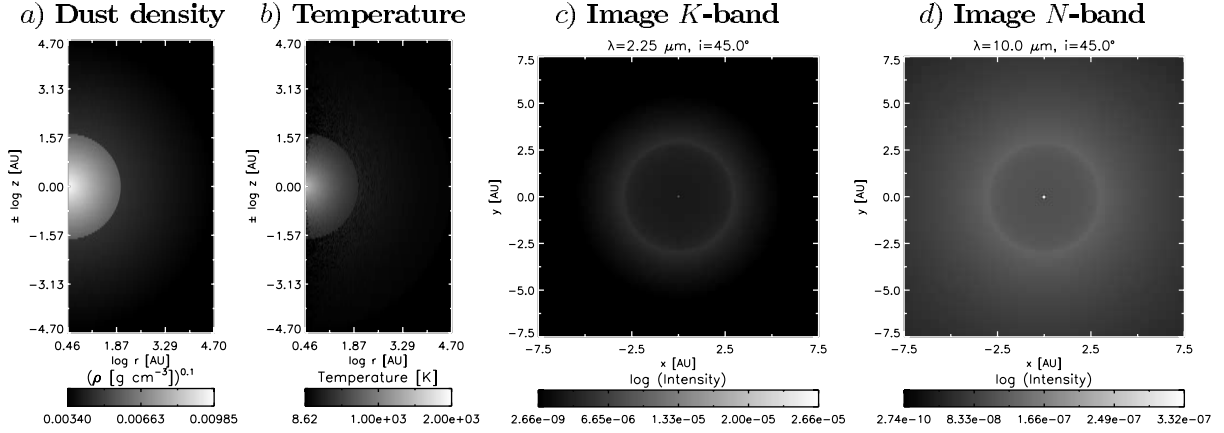
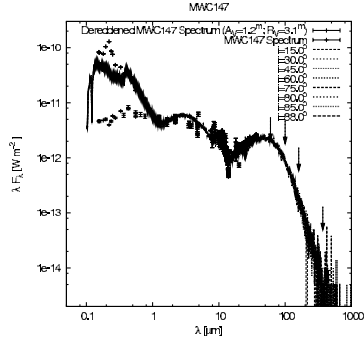


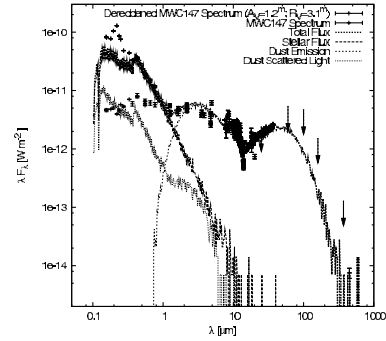
FIG. 10.— Analytic accretion disk model, assuming the Hillenbrand et al. (1992) disk temperature profile ( $\chi^2 = 5.56$ ). Panels *a* and *b* show the corresponding brightness distribution for two representative NIR ( $2.25 \mu\text{m}$ ) and MIR ( $10.0 \mu\text{m}$ ) wavelengths. Panel *c* shows the SED for various inclination angles, whereas panel *d* gives the SED for the best-fit inclination angle and separates the flux that originates in stellar photospheric emission and from the accretion disk. Finally, panels *e* and *f* depict the NIR and MIR visibilities. [See the electronic edition of the Journal for a color version of this figure.]



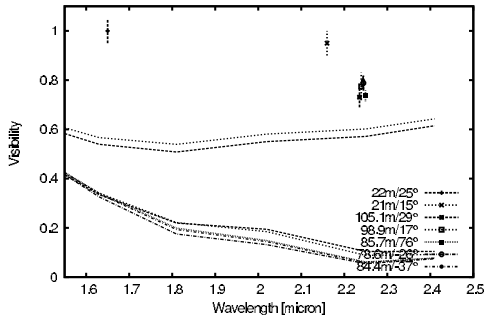
e) SED (different incl.)



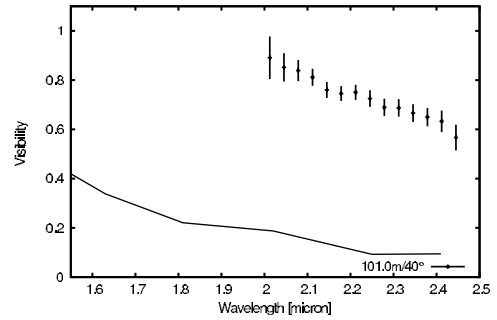
f) SED (details)



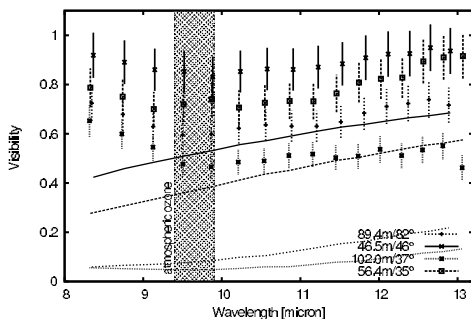
g) Visibilities NIR (IOTA/PTI)



h) Visibilities NIR (AMBER)



i) Visibilities MIR (MIDI)



j) Visibilities MIR (MIDI)

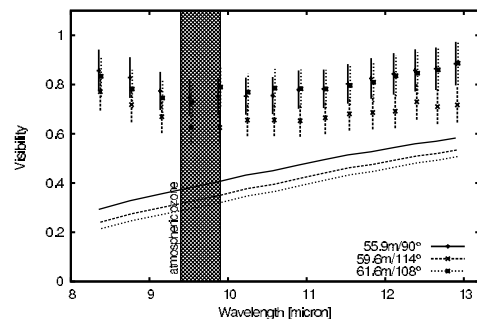


FIG. 11.—Radiative transfer model computed for MWC 147 assuming a spherical shell geometry (model SHELL,  $\chi_r^2 = 80.2$ ; see § 4.2 for a model description). For the model parameters, see Table 6. In panels a and b, we show the dust density and the temperature distribution. Panels c and d show the ray-traced images for two representative NIR (2.25  $\mu\text{m}$ ) and MIR (10.0  $\mu\text{m}$ ) wavelengths. Panel e shows the SED for various inclination angles, whereas panel f gives the SED for the best-fit inclination angle and separates the flux which originates in stellar photospheric emission, thermal emission, dust irradiation, and accretion luminosity. Finally, panels g and h depict the NIR and MIR visibilities computed from our radiative transfer models. [See the electronic edition of the Journal for a color version of this figure.]

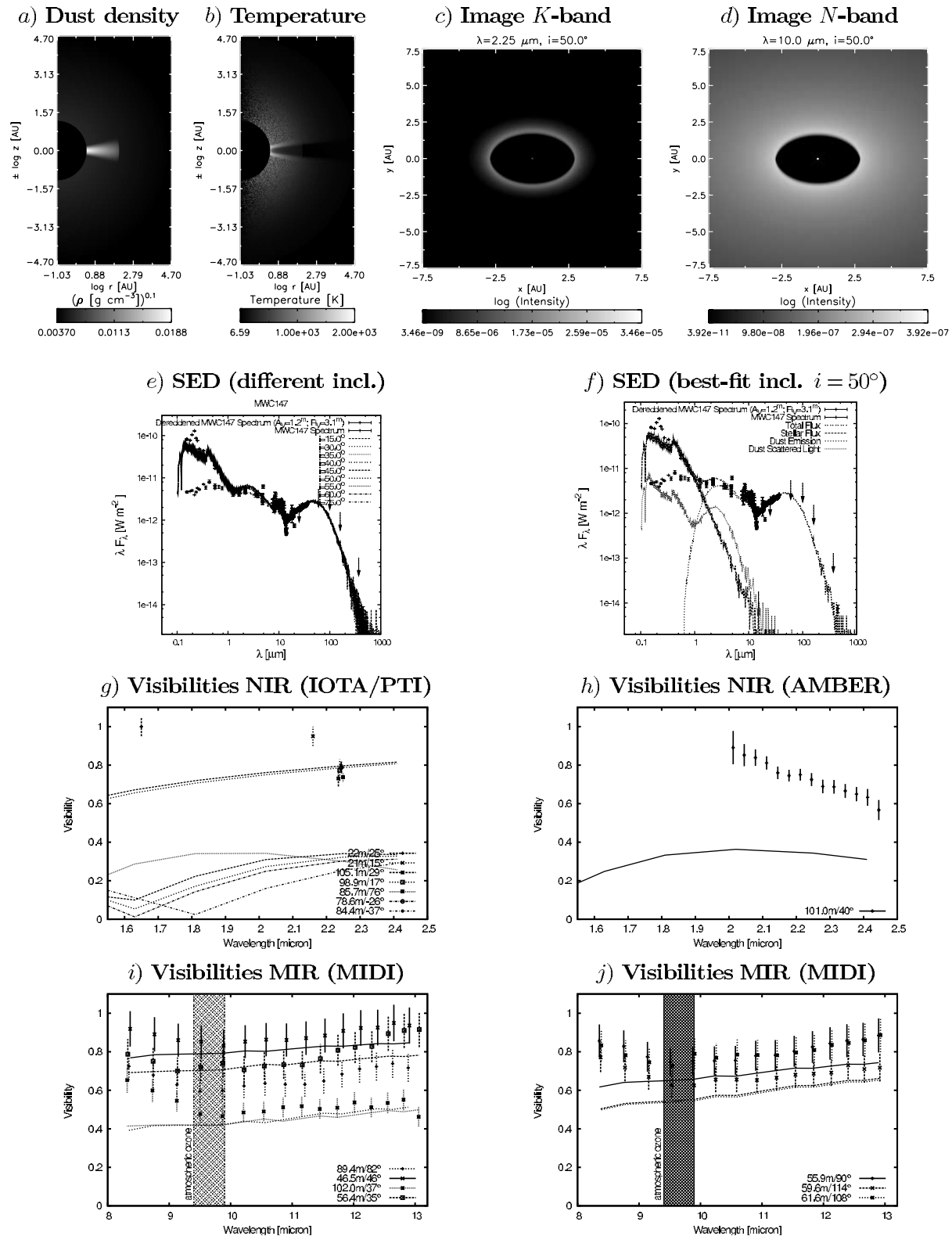


FIG. 12.— Similar to Fig. 11, but showing the radiative transfer model for a flared Keplerian disk geometry with a vertical inner rim (model VERT-RIM,  $\chi_r^2 = 25.3$ ; see § 4.3 for a model description). [See the electronic edition of the Journal for a color version of this figure.]

and photometric data from the literature) to constrain our radiative transfer models. The contribution of the visual companion (Baines et al. 2006; separation  $3.1''$ ) to the SED is unknown. Furthermore, the photometric data may be contaminated by the ambient reflection nebula NGC 2247 (Casey 1991). Polomski et al.

(2002) studied the appearance of the circumstellar environment of MWC 147 at MIR wavelengths and found an extended structure of  $\sim 12''$  diameter ( $\sim 9600$  AU) at  $10 \mu\text{m}$ .

In the course of our modeling of the SED of MWC 147, we found that disk models are not able to reproduce the

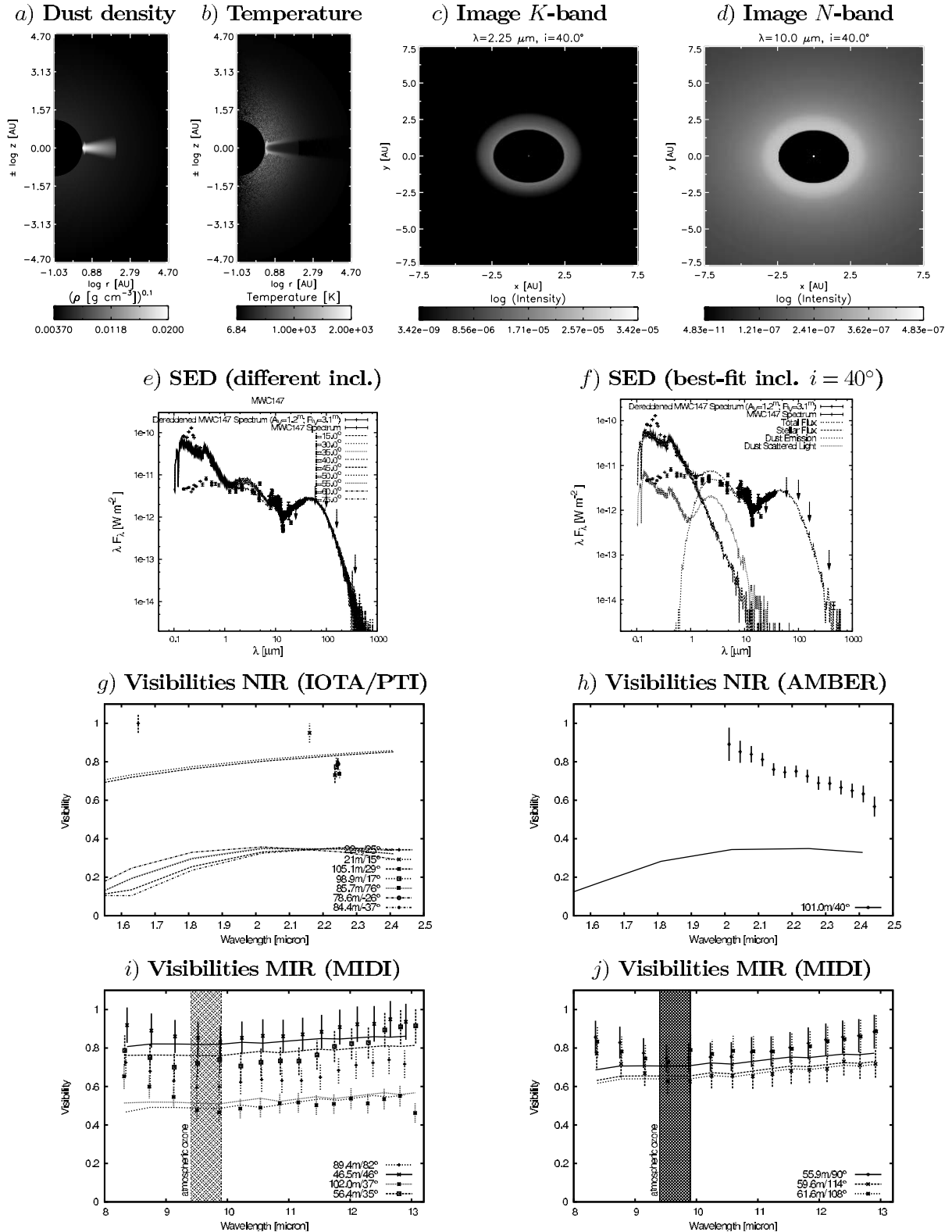


FIG. 13.— Similar to Fig. 11, but showing the radiative transfer model for a flared Keplerian disk geometry with a curved puffed-up inner rim (model CURV-RIM,  $\chi_r^2 = 20.9$ ; see § 4.3 for a model description). [See the electronic edition of the Journal for a color version of this figure.]

observed SED longward of  $15 \mu\text{m}$  (see Fig. 6). The large observed fluxes at mid- and far-infrared (FIR) wavelengths require the presence of an extended envelope. We tried various geometries for this envelope, including rotating, infalling envelopes with and without polar outflow cavities, as used by Whitney et al. (2003). However, the best agreement was ob-

tained for a simple power-law dust distribution with a rather flat slope,

$$\rho_{\text{env}}(r) = \rho_0 \left( \frac{r}{r_0} \right)^{-1/2} \times F(r_{\text{cutoff}}), \quad (2)$$

where  $\rho_0$  is the dust density at some characteristic radius  $r_0$ .

TABLE 6  
PARAMETERS AND FITTING RESULTS FOR OUR TWO-DIMENSIONAL RADIATIVE TRANSFER MODELS

Parameter	SHELL (Fig. 11)	VERT-RIM (Fig. 12)	CURV-RIM (Fig. 13)	VERT-RIM-ACC (Fig. 14)	CURV-RIM-ACC (Fig. 15)
Outer radius (AU) .....	100	100	100	100	100
Dust density at 10 AU ( $\text{g cm}^{-3}$ ) <sup>a</sup> ..	$2.8 \times 10^{-21}$	$1.1 \times 10^{-18}$	$1.6 \times 10^{-18}$	$9.4 \times 10^{-19}$	$8.0 \times 10^{-19}$
Grain size distribution <sup>b</sup> .....	Small	Small and large	Small and large	Small and large	Small and large
Radial power law exponent $p$ .....	3/2	15/8	15/8	15/8	15/8
Vertical power law exponent $q$ .....	...	9/8	9/8	9/8	9/8
Mass accretion rate ( $M_{\odot} \text{ yr}^{-1}$ ) <sup>c</sup> .....	...	...	...	$7.0 \times 10^{-6}$	$6.5 \times 10^{-6}$
Inclination (deg) .....	...	50	40	50	40
Best-fit P.A. (deg) .....	...	50	30	80	110
$\chi_r^2$ NIR .....	316.7	135.2	119.4	2.07	2.71
$\chi_r^2$ MIR .....	33.8	3.72	1.60	0.79	0.95
$\chi_r^2$ total .....	80.2	25.3	20.9	0.99	1.24

NOTES.—All models include an extended outer envelope in order to fit the MIR to FIR SED (see § 4.1.2). The envelope is composed of small dust grains, with a density distribution  $\rho \propto r^{-1/2}$  with  $\rho_0 = 3 \times 10^{-23} \text{ g cm}^{-3}$  at  $r_0 = 10 \text{ AU}$  (see eq. [2]). The outer cutoff radius  $r_{\text{cutoff}} = 40\,000 \text{ AU}$  was chosen such that the dust temperature drops below 10 K. For all models, we assume a minimum dust density of  $10^{-25} \text{ g cm}^{-3}$ .

<sup>a</sup> Dust density, as measured at a radius of 10 AU in the disk midplane.

<sup>b</sup> Dust composition—Mixture of warm silicates (Ossenkopf et al. 1992) and amorphous carbon (Hanner 1988) (to equal parts). The size distribution follows  $n(a) \propto a^{-3.5}$ . For *small grains* we choose  $a_{\text{min}} = 0.005 \mu\text{m}$  and  $a_{\text{max}} = 1.0 \mu\text{m}$ , whereas for *large grains* we use  $a_{\text{min}} = 1.0 \mu\text{m}$  and  $a_{\text{max}} = 1000 \mu\text{m}$ .

<sup>c</sup> Inner gaseous disk—The inner gaseous disk component is modeled to be geometrically thin, optically thick, and to extend from the corotation radius  $R_{\text{corot}}$  to the dust sublimation radius (see § 4.4).

The fitting of the SED and the visibilities was done in the following way: First, we fixed the geometry of the extended envelope to match the MIR to the FIR SED. Then, we varied the geometry for the inner component (§§ 4.2 and 4.3) to obtain the best fit to the NIR and MIR SEDs. The SEDs could be reproduced well with any of the geometrical models considered below, again demonstrating the highly ambiguous nature of SED fits. Significant deviations between the model SEDs and the observed SED are only apparent in the UV spectral range, between  $\sim 150$  and  $\sim 300 \text{ nm}$ . The observed UV excess is related to accretion activity and originates probably from the shocks where accreted material crashes onto the stellar surface. As these accretion shocks are not included in our modeling, we ignore the SED deviations in the UV spectral range.

Finally, the agreement of the model with the interferometric observables was tested. The analytic model fits presented in Table 5 indicate that the disk should be notably inclined ( $\sim 40^\circ$ – $60^\circ$ ); therefore, we computed each radiative transfer model for different inclinations (from edge-on to face-on with an interval of  $15^\circ$ ) in order to find the best agreement both with the spectral shape of the SED and the visibilities. In total, about one thousand radiative transfer models have been computed to identify the best-fit models presented in §§ 4.2–4.4.

#### 4.2. Model SHELL: Spherical Shell Geometry

Miroshnichenko et al. 1997 proposed that optically thin shells can reproduce the SED of HAeBe stars. For our spherical shell model we assumed a density distribution given by

$$\rho_{\text{shell}}(r) = \rho_0 \left( \frac{r}{r_0} \right)^{-p} \times F(r_{\text{cutoff}}). \quad (3)$$

with  $p = 3/2$ . As can be seen in Figure 11, the shell model can reproduce the measured SED quite well, but completely fails to reproduce the NIR and MIR visibilities, both the absolute level of the visibilities as well as their spectral dependence. Due to this very poor fit to the interferometric observables ( $\chi_r^2 = 80.2$ ), we can reject this geometry. In addition, spherical models cannot reproduce the elongation revealed by the analytic model fits (see § 3.3).

#### 4.3. Models VERT-RIM & CURV-RIM: Passive Dust Disks

One solution for a passive disk which is gravitationally dominated by the central star, vertically isothermal, and in vertical hydrostatic equilibrium is given by a Keplerian disk geometry (Shakura & Syunyaev 1973) with a density distribution

$$\rho_{\text{disk}}(r, z) = \rho_0 \left( \frac{r}{r_0} \right)^{-p} \exp \left[ -\frac{\pi}{4} \left( \frac{z}{h_z} \right)^2 \right] F(r_{\text{cutoff}}), \quad (4)$$

$$h_z(r) = h_0 r_0 \left( \frac{r}{r_0} \right)^q, \quad (5)$$

where  $r$  is the radial distance in the midplane,  $z$  is the height above the disk midplane, and  $h_z$  is the vertical pressure scale height.  $h_0$  is the relative geometrical thickness of the disk at the characteristic radius  $r_0$ . To reproduce the SED of MWC 147, we find best agreement with a slightly flared disk geometry ( $q = 9/8$ ; Kenyon & Hartmann 1987) and with a radial density power-law exponent  $p = 15/8$  [corresponding to a surface density law  $\Sigma(r) \propto r^{-3/4}$ ].

In the model VERT-RIM, the inner disk edge of the density distribution is simply truncated, resulting in a vertical wall at the dust sublimation radius (Fig. 9b). Natta et al. (2001) and Dullemond et al. (2001) proposed a modification of the disk geometry; namely, a “puffed-up” inner rim. As the dust at the inner rim (at the dust sublimation radius) is directly exposed to the stellar radiation, the scale height in this region will be significantly increased. Isella & Natta (2005) pointed out that  $T_{\text{subl}}$  depends on the gas density, which results in a higher sublimation temperature in the disk midplane than in the disk atmosphere, causing a curved rim shape. Recently, Tannirkulam et al. (2007) investigated also the effect of dust segregation on the rim shape, considering two dust species with different grain sizes that are distributed over different scale heights. Both the pressure-dependent dust sublimation temperature, as well as the dust settling effects, result in a curved shape of the inner dust rim. In order to investigate the influence of this curved rim on our model fit, we use the analytic dust segregation model from Tannirkulam et al. (2007) to compute the dust scale height  $h_z$  at the evaporation front as a function of distance along the disk midplane. We

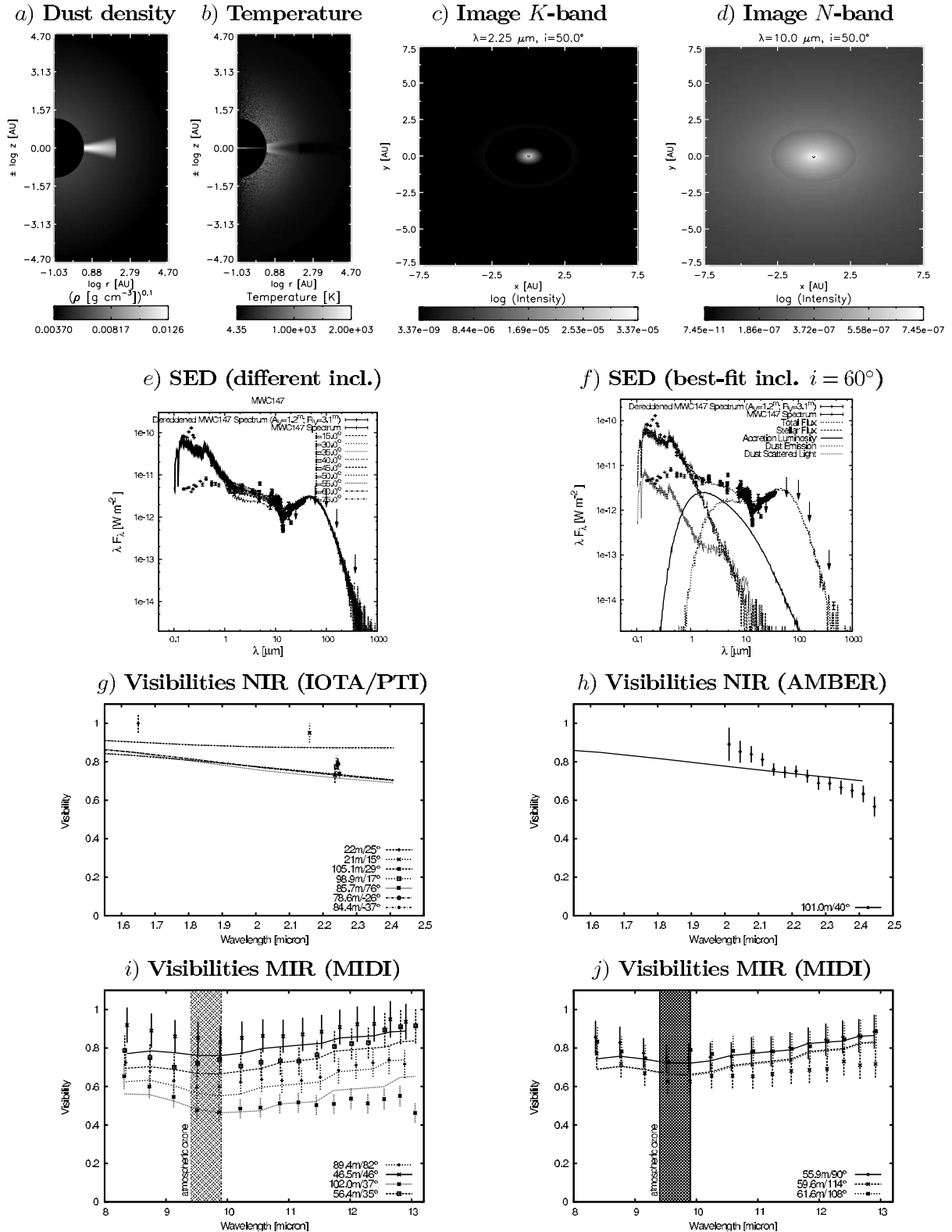


FIG. 14.— Similar to Fig. 11, but showing the radiative transfer model for a flared Keplerian disk geometry with a vertical inner rim, including accretion (model VERT-RIM-ACC,  $\chi^2_r = 0.99$ ; see § 4.4 for a model description). [See the electronic edition of the Journal for a color version of this figure.]

use the Planck mean opacities corresponding to the two dust species described in § 4.1.1, and assume that larger grain species has settled to 60% of the scale height of the smaller grain population (Tannirkulam et al. 2007). The computed scale height for the curved rim is combined with the scale height of the outer flared disk, providing the input density distribution for our ra-

diative transfer simulation of a disk model with curved inner rim (model CURV-RIM; Fig. 9c).

For all models with irradiated disks, we find that especially the NIR model visibilities are always much smaller than the measured visibilities (see Fig. 12 and 13). A similar, although less pronounced, deviation was found in the MIR visibilities.

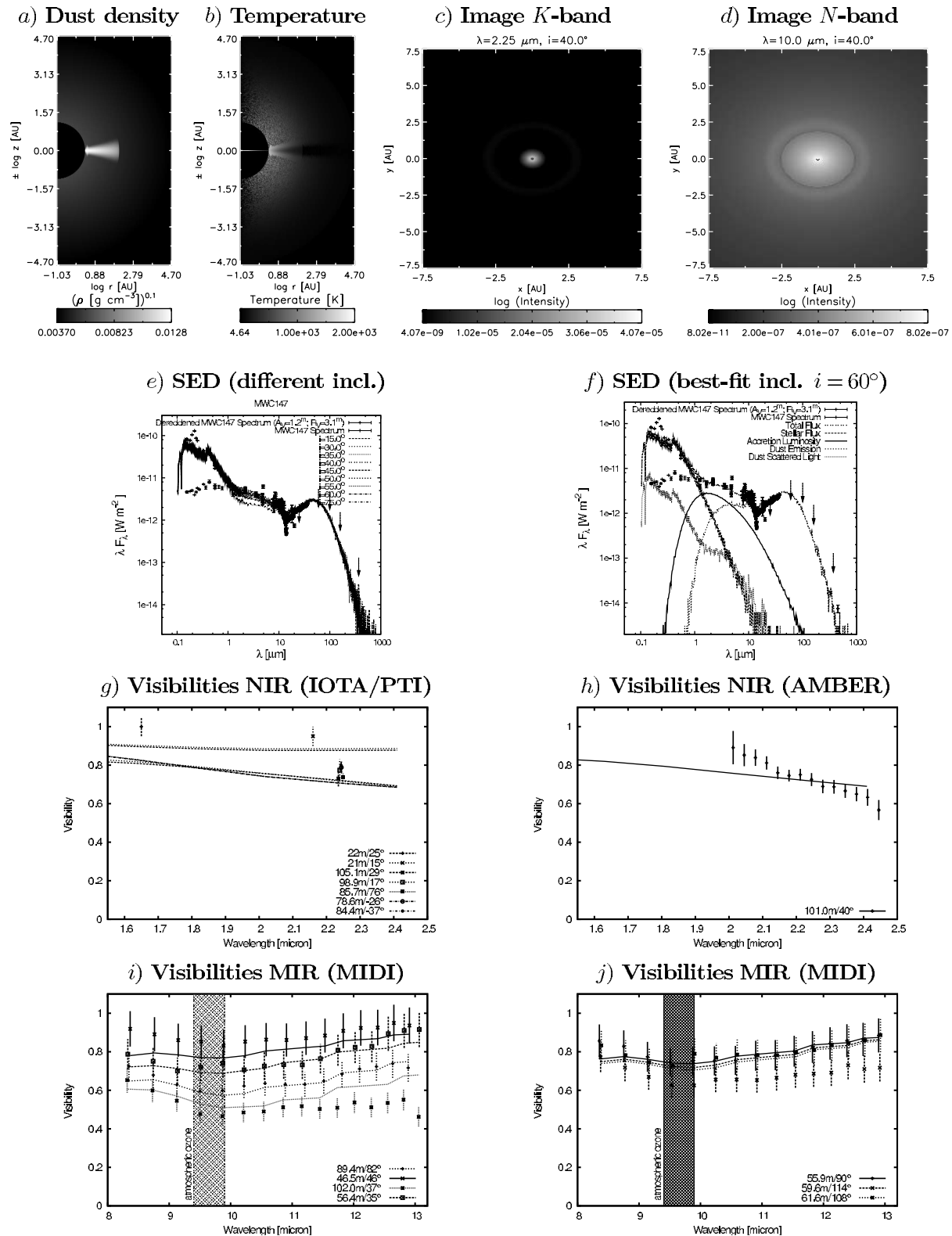


FIG. 15.— Similar to Fig. 11, but showing the radiative transfer model for a flared Keplerian disk geometry with a curved puffed-up inner rim, including accretion (model CURV-RIM-ACC,  $\chi_r^2 = 1.24$ ; see § 4.4 for a model description). [See the electronic edition of the Journal for a color version of this figure.]

Therefore, the radiative transfer modeling confirms and quantifies the general tendency already observed in the geometric model fits; namely, that without considering accretion luminosity, the measured NIR radius of  $\sim 0.7$  AU (see Table 4) is a factor of 4 smaller than the dust sublimation radius. We conclude that although passive irradiated circumstellar disk models are able to

reproduce the SED of MWC 147, these models are in strong conflict with the interferometric measurements (resulting in  $\chi_r^2 = 25.3$  for model VERT-RIM and  $\chi_r^2 = 20.9$  for model CURV-RIM; see Table 6 and Figs. 12 and 13). We would like to point out that adding even larger dust grains cannot solve this discrepancy, since for grain sizes  $\geq 1.2 \mu\text{m}$  the inner rim location becomes

practically independent of the grain size distribution (see discussion in Isella et al. 2006).

#### 4.4. Models VERT-RIM-ACC and CURV-RIM-ACC: Dust Disks with Active Inner Gaseous Accretion Disk

In passive circumstellar disks, the infrared emission is generally assumed to originate almost entirely from dust; the emissivity of the inner dust-free gaseous part of the disk, at radii smaller than the dust sublimation radius, is negligible. In an actively accreting disk, on the other hand, viscous dissipation of energy in the inner dust-free gaseous part of the accretion disk can heat the gas to high temperatures and give rise to significant amounts of infrared emission from optically thick gas. The inner edge of this gas accretion disk is expected to be located a few stellar radii above the stellar surface, where the hot gas is thought to be channeled toward the star via magnetospheric accretion columns. While the magnetospheric accretion columns are too small to be resolved in our interferometric data ( $3 R_*$  correspond to 0.09 AU or 0.12 mas), the infrared emission from hot gas inside the dust sublimation radius should be clearly distinguishable from the thermal emission from the dusty disk due to the different temperatures of these components and the resulting characteristic slope in the NIR- and MIR-visibilitys.

As MWC 147 is a quite strong accretor ( $\dot{M}_{\text{acc}} \approx 10^{-5} M_{\odot} \text{ yr}^{-1}$ ; Hillenbrand et al. 1992), infrared emission from the inner gaseous accretion disk is likely. Muzerolle et al. (2004) found that even for smaller accretion rates the gaseous inner accretion disk is several times thinner than the puffed-up inner dust disk wall and is optically thick (both in radial as well as in the vertical direction).

To include the thermal emission from the inner gaseous disk in our radiative transfer models, we use a similar approach as Akeson et al. (2005). We assume that the accretion luminosity is emitted from a viscous accretion disk (Pringle 1981), which emits at each radius  $r$  as a blackbody of temperature

$$T_{\text{gas}}^4(r) = \left( \frac{3GM_*\dot{M}}{8\pi\sigma r^3} \right) \left( 1 - \sqrt{R_*/r} \right)^{1/2}. \quad (6)$$

We run  $r$  from the magnetic truncation radius  $R_{\text{corot}}$  to the dust sublimation radius. To estimate  $R_{\text{corot}}$  for MWC 147, we use the measured rotation velocity ( $v \sin i = 90 \text{ km s}^{-1}$ ; Boehm & Catala 1995), the stellar parameters from Table 1, and an intermediate inclination angle (as derived from the geometric model fits in Table 5,  $i = 60^\circ$ ), and yield  $R_{\text{corot}} = GM_*/(2\pi v^2) \approx 3R_*$ . In our Monte Carlo radiative transfer simulation, the photons from the gaseous accretion disk are emitted isotropically from the disk midplane and then propagate through the simulation grid. In the course of a simulation, the accretion disk is assumed to be totally optically thick. Another possible consequence of the presence of an optically thick inner gas disk may be shielding of the inner dust rim, allowing dust to exist closer to the star. However, based on the results of the theoretical work by Muzerolle et al. (2004), we consider this to be a secondary effect and do not include it in our modeling. In order to reproduce the SED in the presence of the excess infrared continuum emission from optically thick gas, we vary the fraction between small and large dust grains in the disk in radial direction, which is in qualitative agreement with the indications for grain growth found in the inner disk regions (§ 3.2).

Including the accretion luminosity from an inner gaseous disk improves the agreement between model predictions and observed visibilitys considerably. With a flared disk geometry and an accretion rate of  $\dot{M}_{\text{acc}} = 7 \times 10^{-6} M_{\odot} \text{ yr}^{-1}$  (see Table 6), both the SED and the interferometric visibilitys (Figs. 14 and 15) are reasonably well reproduced. This result is not very sensitive to

the precise shape of the inner rim (model VERT-RIM-ACC:  $\chi_r^2 = 0.99$ ; model CURV-RIM-ACC:  $\chi_r^2 = 1.24$ ).

## 5. CONCLUSIONS

We have presented infrared long-baseline interferometric observations of MWC 147, constraining, for the first time, the inner circumstellar environment around a Herbig Be star over the wavelength range from 2 to 13  $\mu\text{m}$ .

The interferometric data obtained from the PTI archive and with VLTI/AMBER suggest a characteristic diameter of just  $\sim 1.3$  AU (Gaussian FWHM) for the NIR emitting region, while the MIR structure is about a factor of 7 more extended (9 AU at 11  $\mu\text{m}$ ). Within the  $K$  band, we measure a significant increase of size with wavelength. Comparing the measured wavelength dependence of the characteristic size with the class of analytic accretion disk models, which are currently most commonly applied for the modeling of HAeBe SEDs (Hillenbrand et al. (1992) and NIR interferometric data (e.g., Vinković & Jurkić 2007) yields that these models cannot well reproduce the measured significant increase of the apparent size with wavelength. To test whether more realistic physical models of the circumstellar dust environment yield better agreement, we employed two-dimensional radiative transfer modeling. The radiative transfer models were constructed to fit the SED from 0.3 to 450  $\mu\text{m}$ , including an extended envelope and an inner dust shell/disk geometry. While models of passive irradiated disks with or without puffed-up rims are able to reproduce the SED, they are in conflict with the interferometric observables, significantly overestimating the size of both the NIR and MIR emission. This is also the case, to an even bigger extend, for spherical shell geometries. Therefore, in our radiative transfer models, we incorporated additional accretion luminosity emitted from an inner gaseous disk, yielding significantly better agreement with the interferometric data. The best-fit was obtained with a flared Keplerian disk seen under an inclination of  $\sim 50^\circ$ , extending out to 100 AU and exhibiting a mass accretion rate of  $7 \times 10^{-6} M_{\odot} \text{ yr}^{-1}$ .

Since MWC 147 belongs to the group of “undersized” Herbig Be star disks (which have measured NIR diameters smaller than expected from the size-luminosity relation; see Monnier et al. 2005), our detailed spectrointerferometric study confirms earlier speculations that the NIR emission of Herbig Be stars in this group might be dominated by gas emission from inside the dust sublimation radius.

Furthermore, our study demonstrates that the spectrointerferometric capabilities of the latest generation of long-baseline interferometric instruments are particularly well suited to reveal the contributions from active accretion processes taking place close to the star. To achieve further progress on MWC 147, it seems promising for future spectrointerferometric observations not only to extend the spectral coverage (e.g., to the  $J$ - and  $H$  band) but to employ also a higher spectral resolution in order to study the spatial origin of accretion-related emission lines (e.g., Br $\gamma$ ; Garcia Lopez et al. 2006), maybe tracing ionized, optically thin gas in the disk or magnetospheric accretion (Hartmann et al. 1994). In addition, future long-baseline interferometric observations will measure the closure phase relation, which is a sensitive measure to asymmetries in the source brightness distribution, and which provides also the key to direct aperture synthesis imaging of the sub-AU circumstellar environment.

We thank Thomas Driebe, who developed software tools which were used in the course of the reduction of the VLTI/MIDI

data. We are also grateful to Rachel Akeson for advice on the reduction of the PTI data, and to the anonymous referee, whose detailed referee report helped to improve this paper. S. K. was supported for this research through a fellowship from the International Max Planck Research School (IMPRS) for Radio and Infrared Astronomy at the University of Bonn.

The Palomar Testbed Interferometer is operated by the Michelson Science Center and the PTI collaboration and was constructed with funds from the Jet Propulsion Laboratory, Caltech as provided by the National Aeronautics and Space Administration. This work has made use of services produced by the Michelson Science Center at the California Institute of Technology.

This work is based, in part, on archival data obtained with the *Spitzer Space Telescope*, which is operated by the Jet Propulsion Laboratory, California Institute of Technology under a contract with NASA.

SMART was developed by the IRS Team at Cornell University and is available through the *Spitzer* Science Center at Caltech.

This publication makes use of data products from the Two Micron All Sky Survey, which is a joint project of the University of Massachusetts and the Infrared Processing and Analysis Center/California Institute of Technology, funded by the National Aeronautics and Space Administration and the National Science Foundation.

## REFERENCES

- Acke, B., & van den Ancker, M. E. 2004, *A&A*, 426, 151  
 Akeson, R. L., Ciardi, D. R., van Belle, G. T., Creech-Eakman, M. J., & Lada, E. A. 2000, *ApJ*, 543, 313  
 Akeson, R. L., et al. 2005, *ApJ*, 622, 440  
 Allamandola, L. J., Tielens, A. G. G. M., & Barker, J. R. 1985, *ApJ*, 290, L25  
 Baines, D., Oudmaijer, R. D., Porter, J. M., & Pozzo, M. 2006, *MNRAS*, 367, 737  
 Berrilli, F., Lorenzetti, D., Saraceno, P., & Strafella, F. 1987, *MNRAS*, 228, 833  
 Bertout, C., Robichon, N., & Arenou, F. 1999, *A&A*, 352, 574  
 Bjorkman, J. E., & Wood, K. 2001, *ApJ*, 554, 615  
 Boehm, T., & Catala, C. 1995, *A&A*, 301, 155  
 Bouret, J.-C., Martin, C., Deleuil, M., Simon, T., & Catala, C. 2003, *A&A*, 410, 175  
 Brittain, S. D., Simon, T., Najita, J. R., & Rettig, T. W. 2007, *ApJ*, 659, 685  
 Casey, S. C. 1991, *ApJ*, 371, 183  
 Cohen, M. 1973, *MNRAS*, 161, 105  
 Colavita, M. M., et al. 1999, *ApJ*, 510, 505  
 Corporon, P., & Lagrange, A.-M. 1999, *A&AS*, 136, 429  
 Dullemond, C. P., Dominik, C., & Natta, A. 2001, *ApJ*, 560, 957  
 Egan, M. P., Price, S. D., Shipman, R. F., Gugliotti, G. M., Tedesco, E. F., Moshir, M., & Cohen, M. 1999, in *ASP Conf. Ser. 177, Astrophysics with Infrared Surveys: A Prelude to SIRTF*, ed. M. D. Bica, R. M. Cutri, & B. F. Madore (San Francisco: ASP), 404  
 Egret, D., Delidon, P., McLean, B. J., Russell, J. L., & Turon, C. 1992, *A&A*, 258, 217  
 Eisner, J. A., Chiang, E. I., Lane, B. F., & Akeson, R. L. 2007, *ApJ*, 657, 347  
 Eisner, J. A., Hillenbrand, L. A., White, R. J., Akeson, R. L., & Sargent, A. I. 2005, *ApJ*, 623, 952  
 Eisner, J. A., Lane, B. F., Hillenbrand, L. A., Akeson, R. L., & Sargent, A. I. 2004, *ApJ*, 613, 1049  
 Friedjung, M. 1985, *A&A*, 146, 366  
 Garcia Lopez, R., Natta, A., Testi, L., & Habart, E. 2006, *A&A*, 459, 837  
 Habart, E., Natta, A., & Krügel, E. 2004, *A&A*, 427, 179  
 Habart, E., Natta, A., Testi, L., & Carillet, M. 2006, *A&A*, 449, 1067  
 Hanner, M. 1988, *Grain Optical Properties* (Washington: NASA)  
 Hartmann, L., Hewett, R., & Calvet, N. 1994, *ApJ*, 426, 669  
 Helou, G., & Walker, D. W., ed. 1988, *Infrared Astronomical Satellite (IRAS) Catalogs and Atlases, Volume 7, The Small Scale Structure Catalog (NASA RP-1190)*; Washington: NASA)  
 Hernández, J., Calvet, N., Briceño, C., Hartmann, L., & Berlind, P. 2004, *AJ*, 127, 1682  
 Higdon, S. J. U., et al. 2004, *PASP*, 116, 975  
 Hillenbrand, L. A., Strom, S. E., Vrba, F. J., & Keene, J. 1992, *ApJ*, 397, 613  
 Hinz, P. M., Hoffmann, W. F., & Hora, J. L. 2001, *ApJ*, 561, L131  
 Høg, E., et al. 2000, *A&A*, 355, L27  
 Hönig, S. F., Beckert, T., Ohnaka, K., & Weigelt, G. 2006, *A&A*, 452, 459  
 Houck, J. R., et al. 2004, *ApJS*, 154, 18  
 Isella, A., & Natta, A. 2005, *A&A*, 438, 899  
 Isella, A., Testi, L., & Natta, A. 2006, *A&A*, 451, 951  
 Jaffe, W. J. 2004, *Proc. SPIE*, 5491, 715  
 Jain, S. K., Bhatt, H. C., & Sagar, R. 1990, *A&AS*, 83, 237  
 Kenyon, S. J., & Hartmann, L. 1987, *ApJ*, 323, 714  
 Kraus, S., et al. 2005, *AJ*, 130, 246  
 Kurucz, R. L. 1970, *SAO Special Report 308* (Cambridge: SAO)  
 Leinert, C., et al. 2004, *A&A*, 423, 537  
 Lynden-Bell, D., & Pringle, J. E. 1974, *MNRAS*, 168, 603  
 Malbet, F., et al. 1998, *ApJ*, 507, L149  
 ———. 2007, *A&A*, 464, 43  
 Mannings, V. 1994, *MNRAS*, 271, 587  
 Mathis, J. S., Rumpl, W., & Nordsieck, K. H. 1977, *ApJ*, 217, 425  
 Mérand, A., Bordé, P., & Coudé Du Foresto, V. 2005, *A&A*, 433, 1155  
 Millan-Gabet, R., Schloerb, F. P., & Traub, W. A. 2001, *ApJ*, 546, 358  
 Millan-Gabet, R., Schloerb, F. P., Traub, W. A., Malbet, F., Berger, J. P., & Bregman, J. D. 1999, *ApJ*, 513, L131  
 Min, M., Dominik, C., Hovenier, J. W., de Koter, A., & Waters, L. B. F. M. 2006, *A&A*, 445, 1005  
 Miroshnichenko, A., Ivezić, Z., & Elitzur, M. 1997, *ApJ*, 475, L41  
 Miroshnichenko, A., Ivezić, Z., Vinković, D., & Elitzur, M. 1999, *ApJ*, 520, L115  
 Monnier, J. D., & Millan-Gabet, R. 2002, *ApJ*, 579, 694  
 Monnier, J. D., et al. 2005, *ApJ*, 624, 832  
 Muzerolle, J., D'Alessio, P., Calvet, N., & Hartmann, L. 2004, *ApJ*, 617, 406  
 Natta, A., & Kruegel, E. 1995, *A&A*, 302, 849  
 Natta, A., Prusti, T., Neri, R., Wooden, D., Grinin, V. P., & Mannings, V. 2001, *A&A*, 371, 186  
 Nisini, B., Milillo, A., Saraceno, P., & Vitali, F. 1995, *A&A*, 302, 169  
 Ohnaka, K., et al. 2006, *A&A*, 445, 1015  
 Oliver, R. J., Masheder, M. R. W., & Thaddeus, P. 1996, *A&A*, 315, 578  
 Ossenkopf, V., Henning, T., & Mathis, J. S. 1992, *A&A*, 261, 567  
 Pasinetti Fracassini, L. E., Pastori, L., Covino, S., & Pozzi, A. 2001, *A&A*, 367, 521  
 Petrov, R. G., et al. 2003, *Proc. SPIE*, 4838, 924  
 ———. 2007, *A&A*, 464, 1  
 Polomski, E. F., Telesco, C. M., Piña, R., & Schulz, B. 2002, *AJ*, 124, 2207  
 Preibisch, T., Kraus, S., Driebe, T., van Boekel, R., & Weigelt, G. 2006, *A&A*, 458, 235  
 Pringle, J. E. 1981, *ARA&A*, 19, 137  
 Przygodda, F., Chesneau, O., Graser, U., Leinert, C., & Morel, S. 2003, *Ap&SS*, 286, 85  
 Rho, J., Reach, W. T., Lefloch, B., & Fazio, G. G. 2006, *ApJ*, 643, 965  
 Richichi, A., & Percheron, I. 2002, *A&A*, 386, 492  
 Richichi, A., Percheron, I., & Khristoforova, M. 2005, *A&A*, 431, 773  
 Shakura, N. I., & Syunyaev, R. A. 1973, *A&A*, 24, 337  
 Skinner, S. L., Brown, A., & Stewart, R. T. 1993, *ApJS*, 87, 217  
 Skrutskie, M. F., et al. 2006, *AJ*, 131, 1163  
 Tannirkulam, A., Harries, T. J., & Monnier, J. D. 2007, *ApJ*, 661, 374  
 Tatulli, E., et al. 2007, *A&A*, 464, 29  
 Thompson, G. I., Nandy, K., Jamar, C., Monfils, A., Houziaux, L., Carnochan, D. J., & Wilson, R. 1978, *Catalogue of Stellar Ultraviolet Fluxes* (London: SRC)  
 Turon, C., et al. 1993, *Bull. Inf. Cent. Donnees Astron.*, 43, 5  
 Tuthill, P. G., Monnier, J. D., Danchi, W. C., Hale, D. D. S., & Townes, C. H. 2002, *ApJ*, 577, 826  
 van Boekel, R., et al. 2004a, *Nature*, 432, 479  
 van Boekel, R., Waters, L. B. F. M., Dominik, C., Dullemond, C. P., Tielens, A. G. G. M., & de Koter, A. 2004b, *A&A*, 418, 177  
 van den Ancker, M. E. 2005, in *High Resolution Infrared Spectroscopy in Astronomy*, ed. H. U. Käufel, R. Siebenmorgen, & A. F. M. Moorwood (Dordrecht: Springer), 309  
 van den Ancker, M. E., de Winter, D., & Tjin A Djie, H. R. E. 1998, *A&A*, 330, 145  
 van Dishoeck, E. F. 2004, *ARA&A*, 42, 119  
 Vieira, S. L. A., & Cunha, N. C. S. 1994, *Inf. Bull. Variable Stars*, 4090, 1  
 Vinković, D., Ivezić, Z., Jurkić, T., & Elitzur, M. 2006, *ApJ*, 636, 348  
 Vinković, D., & Jurkić, T. 2007, *ApJ*, 658, 462  
 Wesselius, P. R., van Duinen, R. J., de Jonge, A. R. W., Aalders, J. W. G., Luinge, W., & Wildeman, K. J. 1982, *A&AS*, 49, 427  
 Whitney, B. A., Wood, K., Bjorkman, J. E., & Wolff, M. J. 2003, *ApJ*, 591, 1049  
 Wilkin, F. P., & Akeson, R. L. 2003, *Ap&SS*, 286, 145